

Acquisitions and Bibliographic Services Branch

395 Wellington Street Ottawa, Ontario K1A 0N4 Bibliothèque nationale du Canada

Direction des acquisitions et des services bibliographiques

395, rue Wellington Ottawa (Ontano) K1A 0N4

Your tile. Votre reference

Our tile. Notice reference

NOTICE

The quality of this microform is heavily dependent upon the quality of the original thesis submitted for microfilming. Every effort has been made to ensure the highest quality of reproduction possible.

La quaiité de cette microforme dépend grandement de la qualité de la thèse soumise au microfilmage. Nous avons tout fait pour assurer une qualité supérieure de reproduction.

AVIS

If pages are missing, contact the university which granted the degree.

S'il manque des pages, veuillez communiquer avec l'université qui a conféré le grade.

Some pages may have indistinct print especially if the original pages were typed with a poor typewriter ribbon or if the university sent us an inferior photocopy. La qualité d'impression de certaines pages peut laisser à désirer, surtout si les pages originales ont été dactylographiées à l'aide d'un ruban usé ou si l'université nous a fait parvenir une photocopie de qualité inférieure.

Reproduction in full or in part of this microform is governed by the Canadian Copyright Act, R.S.C. 1970, c. C-30, and subsequent amendments.

La reproduction, même partielle, de cette microforme est soumise à la Loi canadienne sur le droit d'auteur, SRC 1970, c. C-30, et ses amendements subséquents.

Canada

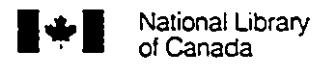
Two specific applications of semi-classical theories in Nuclear Physics

by Juan Gallego

A thesis submitted to the Faculty of Graduate Studies and Research in partial fulfillment of the requirements for the degree of Philosophiae Doctor in Physics.

Department of Physics McGill University Montréal, Québec Canada

December 1993



Acquisitions and Bibliographic Services Branch

395 Wellington Street Ottawa, Ontario K1A 0N4 Bibliothèque nationale du Canada

Direction des acquisitions et des services bibliographiques

395, rue Wellington Ottawa (Ontano) K1A 0N4

Your Ne. Votre reterence

Our file. Notre référence

The author has granted an irrevocable non-exclusive licence allowing the National Library of Canada to reproduce, loan, distribute or sell copies of his/her thesis by any means and in any form or format, making this thesis available to interested persons.

L'auteur a accordé une licence irrévocable et non exclusive à la Bibliothèque permettant nationale du Canada reproduire, prêter, distribuer ou vendre des copies de sa thèse de quelque manière et sous quelque forme que ce soit pour mettre des exemplaires de cette thèse à la disposition des personnes intéressées.

The author retains ownership of the copyright in his/her thesis. Neither the thesis nor substantial extracts from it may be printed or otherwise reproduced without his/her permission. L'auteur conserve la propriété du droit d'auteur qui protège sa thèse. Ni la thèse ni des extraits substantiels de celle-ci ne doivent être imprimés ou autrement reproduits sans son autorisation.

ISBN 0-315-94621-0



Abstract

Two problems in Nuclear Physics are investigated using microscopic semi-classical models. The first model, developed to study heavy ion collisions, is based on the Boltzmann-Uehling-Uhlenbeck theory and has been extended to include one-body fluctuations. It has been successfully applied at low and intermediate energies and a comparison between simulations and an experiment done at the Michigan State University cyclotron facility has yielded very good agreement. The second is a nuclear structure model based on the Thomas-Fermi theory and describes nuclear rotations. It has been used to calculate nuclear shapes and limiting angular momenta across the periodic table. It has been found that it breaches the gap between classical Liquid Drop calculations and quantum Hartree-Fock calculations. Agreement with experimental results is satisfactory.

Resumé

Deux problèmes de Physique nucléaire sont traités avec des modèles microscopiques semi-classiques. Le premier est appliqué aux collisions d'ions lourds à des bases et moyennes énergies. Il est basé sur la théorie de Boltzmann, Uehling et Uhlenbeck modifiée pour traiter des fluctuations à un corps. Des comparaisons faites entre le modèle et des données d'une expérience réalisée au cyclotron à Michigan State University ont été très satisfaisantes. Le deuxième modèle sert à étudier des noyaux en rotation et est basé sur la théorie de Thomas-Fermi. Les résultats obtenus permettent de rapprocher les prédictions du modèle classique de la goute liquide avec celles des modèles quantiques.

Acknowledgements

Many are the people that have contributed one way or another to the completion of this thesis. Foremost I would like to thank my thesis supervisor Dr. S. Das Gupta, without whose help, guidance and, above all, patience this thesis would have never been finished. Not only has he taught me theoretical Nuclear Physics, but also how scientific research is done, and how rewarding it is. I am also grateful to him for making it possible for me to meet some of the other renowned experts in this field.

I would also like to thank Drs. C. Gale, N. detakacsy and S. J. Lee for the many discussions on different aspects of Nuclear Physics. Dr. C. Prunneau spent long hours explaining to me how the MSU detector worked, which helped immensely when I compared our results with their data. P. Mercure made sure that our computer network was always functional, allowing me to get the many CPU cycles that my research required.

I am specially grateful to Sonia Brock, Nuria Gallego and Dolors Planas, for without their support, encouragement and understanding throughout the writing of this thesis, it would have never been completed. Finally, I would like to thank Jean-François Malouin, François Begin, Charles Hooge, Colin Holmes and Hugo Beltrami for the countless hours we have spent talking about life, the universe and everything else.

Contents

In	trodi	ıction	1		
1	The	BUU equation	6		
	1.1	The Vlasov equation	6		
	1.2	The collision integral	11		
	1.3	The nuclear potential	13		
	1.4	Fragmentation process	18		
2	Numerical solution of the BUU equation				
	2.1	Test Particle Method	22		
	2.2	Lattice Hamiltonian Method	25		
	2.3	The cascade code			
	2.4	BUU: Cascade code plus Vlasov propagation	31		
	2.5	Extended BUU: generating fluctuations			
	2.6	The model	34		
	2.7	Testing our model	37		
3	The	mas-Fermi theory	44		
	3.1	Thomas-Fermi theory for static nuclei	44		
		3.1.1 Derivation of the Thomas-Fermi equations for nuclei	44		
	· .	3.1.2 Implementation of the Thomas-Fermi equation	47		
	3.2	Thomas-Fermi solutions for rotating nuclei	51		
		3.2.1 TF equations for rotating nucleus	51		

	3.2.2	Numerical implementation	54
	3.2.3	Comparison with other models	62
Conc	lusion		66
A P	hase-dia	gram for nuclear matter	68
Refer	ences		71

List of Figures

1.1	Phase diagram for nuclear matter	20
2.1	Inclusive cross-section for $\mathcal{Z}=1$	39
2.2	Inclusive cross-section for $\mathcal{Z}=1$ for different angular bins	40
2.3	Inclusive cross-section for $\mathcal{Z}=1$ for different plastic ball multiplicities	41
2.4	Impact parameter contribution to each ball multiplicity bin	42
2.5	Ball multiplicity M versus charge Z in the forward array	43
3.1	Density profiles for different nuclei using potential 1.43	49
3.2	Density profiles for different nuclei using potential 1.49	50
3.3	Excitation energies for 160 Er as a function of \mathcal{L}_z	56
3.4	Density contours for 126 Ba as a function of \mathcal{L}_z	58
3.5	Deformation characteristics as a function of \mathcal{L}_z for three different nuclei	
	using potential 1.43	59
3.6	Moment of inertia versus angular velocity for three nuclei using poten-	
	tial 1.43	60
3.7	Deformation characteristics as a function of \mathcal{L}_z for three different nuclei	
	using potential 1.49	61

List of Tables

1.1	Potential parameters used in this work	18
1.2	Liquid drop coefficients	19
3.1	Transition values of \mathcal{L}_z for different nuclei	57
3.2	Values of x , $\mathcal{L}_{\rm I}$, $\mathcal{L}_{\rm a}$, $\mathcal{L}_{\rm II}$ and $\mathcal{L}_{\rm b}$	64

Introduction

Over the last fifteen years much work has been done in the development of microscopic models for heavy ion collisions. Until the mid-seventies most of the collision experiments with nucleon-nucleus or α -nucleus systems involved measurements of inclusive cross sections for pions and light nuclei $(p, d, {}^{3}\text{He}, {}^{4}\text{He}, \text{etc.})$, and the models developed to reproduce such data were mostly phenomenological: fireball and firestreak models (see [1] for a review), the sequential decay model of Lynch and Friedman [2], as well as others. Based on quite different assumptions, these models were quite successful in reproducing the data, at least to the extent and accuracy set by experiments.

The insensitivity of these early models to the underlying assumptions prompted the design of more sophisticated experiments (including also nucleus-nucleus systems) aiming at accurate measurements of both differential cross sections and exclusive cross sections for a better part of the range of cluster masses emerging from the collisions. Parallel to the experimental effort, theoreticians turned towards microscopic models of the nucleus describing, in a coherent fashion, both the static and quasistatic properties of isolated nuclei, and the dynamical effects observed in collision experiments. Amongst the latter, the dynamics of nuclear fragmentation has received increasing attention over the years. It is this aspect of heavy ion collisions that prompted the present work.

A very useful picture in the description of heavy ion collisions is that of partic-

ipants and spectators. For non-central collisions at sufficient energy, only some of the nucleons of one of the ions will interact with some of the nucleons in the other. These are known as the participants. The rest will continue almost unhindered by the encounter. These are the spectators. The participant nucleons coalesce and form a region of dense, hot nuclear matter that will then disassemble giving rise to many free mesons, baryons and low mass ions. The spectators will evaporate a few particles but will not totally disintegrate. The qualitative difference between participants and spectators allows to distinguish experimentally between near-central collisions and peripheral collisions.

One of the first fully microscopic models was the cascade model [3]. It is based on the assumption that at high enough energies (from a few hundred MeV to around 2 GeV), the outcome of a reaction is mostly dictated by nucleon-nucleon collisions and that the interaction of the constituents with the nuclear field can be ignored. It is therefore well suited for the study of phenomena in which field effects do not play an important role, such as particle production (mostly mesonic and low-mass baryonic states) and bulk matter distributions (like inclusive cross-sections).

Yet without field interactions much of the physics involved in heavy ion collisions at low and intermediate energies is being left out. Foremost, the cascade code is insensitive to the nuclear equation of state (EOS), which plays an important role at these energies and is solely responsible for the evolution of the spectator nucleons. It also renders the code useless when we want to study fragmentation mechanisms and cluster production. The obvious solution is to turn to nuclear transport models. One of the most successful models is the Boltzmann-Uehling-Uhlenbeck (BUU) equation [4,5] (it is also referred to as the Vlasov-Uehling-Uhlenbeck equation, the Boltzmann-Nordheim equation or the Landau-Vlasov equation). In Chapter 1 we will

derive the two components of the BUU equation: the Vlasov term, which describes the evolution of the nuclear phase-space density under its own mean-field, and the collision integral, which deals with the nucleon-nucleon collisions. We will also discuss the underlying EOS and a toy model describing the fragmentation of the participant nucleons.

The numerical implementation of the BUU equation has received much attention over the last few years. The original BUU code uses the Test Particle Method (TPM) to solve the Vlasov propagation, and the cascade code to solve the collision integral. The underlying EOS is a zero-range Skyrme potential. It has been very successful in the study of the average properties of near-central collisions at intermediate energies such as flow angles, transverse momenta and pion production (see [6] for a review).

But the original BUU is not suited for the study of fragmentation dynamics, since it can only yields average properties. Thus many alternative models have been proposed, such as the Quantum Molecular Dynamics of the Frankfurt group [7] and the Gaussian per particle approach of Boal and collaborators [8]. Other models are extensions of the BUU code, such as the extended BUU used in this work [9], the stochastic BUU model [10] and more recently Randrup's fluctuation model [11].

Despite the inclusion of fluctuations, the extended BUU still suffered from a problem that stemmed from the TPM: non-conservation of energy. For reasons that will be discussed in chapter 2, Vlasov propagation using the TPM method results in a significant energy gain as the simulation proceeds, and to the evaporation of particles, rendering all emerging clusters unstable over long periods of time. These two problems are very severe if one is attempting to study cluster production at low energies. Lenk and Pandharipande [12] proposed an alternative numerical technique known as the Lattice Hamiltonian Method (LHM) that conserves energy exactly and does not suffer from particle evaporation.

Another problem with the original BUU code was that it used zero-range Skyrme potentials. This implies that nuclei in this model have sharp surfaces. Yet theoretical studies of peripheral collisions [13-16] show that the diffuse surfaces of real nuclei play an important role in spectator dynamics. Diffuse surfaces can be generated in two different ways: by adding finite-range interactions in the underlying potential as done by Bonche et al. [15] in their Time-Dependent Hartree-Fock (TDHF) model, or by using Gaussian wave-packets to describe individual nucleons, as done by the GANIL group [17].

Our task was to modify the extended BUU code using the LHM to implement the Vlasov propagation, with proper EOS yielding diffuse surfaces. As a test of our model, we simulated an experiment done at the National Superconducting Cyclotron laboratory in Michigan State University by a collaboration between MSU, Chalk River Laboratories and Université Laval, involving 20 Ne on NaF at 45 MeV/nucleon [19,20]. In particular we studied the $\mathcal{Z}=1$ inclusive distributions and the multiplicity-impact parameter relationship. We found good agreement between our calculation and the experimental results.

The second part of our work is concerned with the Thomas-Fermi theory for rotating nuclei. Thomas-Fermi for static nuclei has been used in nuclear theory for the last 30 years. The original Seyler-Blanchard model [21] has been recently revised by Myers and Swiatecki [22] with substantial additions to the liquid drop model of average nuclear properties. Our interest in Thomas-Fermi theory stemmed from the need to generate self-consistent density distributions when the nuclear potential used had finite-range terms. These distributions could then be used in conjunction with our BUU model [18]. Combining BUU and Thomas-Fermi is justified since both theories

can be considered semi-classical approximations of the full Hartree-Fock quantum theory.

In recent years, much experimental work has been done on high-spin states. Theoretical work dates back almost 20 years with the classical rotating liquid drop model developed by Cohen et al. [23] and perfected by Sierk [24]. In recent years, many quantum calculations have also been done (see [25] and references there in), in particular the cranking quantum calculations of Bonche et al. [26-28]. Since these quantum models are based on Hartree-Fock theory, using the same type of potentials used in static Thomas-Fermi theory, we thought it would be instructive to use Thomas-Fermi theory to describe rotations in nuclei, attempting to link the classical continuum results with the quantum calculations.

The attractive feature of the Thomas-Fermi model is the relative ease with which solutions can be obtained. Although these solutions require quite extensive use of computer resources, they are nonetheless far easier than fully quantal Hartree-Fock. At low angular momentum, it is well known that quantum effects play an important role in collective rotations [29,30], and a semi-classical model can not describe such situations accurately. Yet at high angular momenta, we expect Thomas-Fermi to give more accurate descriptions of the physics involved. We expect our model to be a bridge between the fully quantum and the classical calculations. In chapter 3 we present the Thomas-Fermi model both for static and rotating nuclei, and include a comparison of our results with the classic liquid drop and the cranking model results.

Chapter 1

The BUU equation

1.1 The Vlasov equation

The time dependent Hartree-Fock (TDHF) theory is the most appropriate theory to describe heavy ion collision at low energies [6,31]. We start by defining the single-particle density from a convenient set of single particle states $\{i\}$:

$$\varrho_{ij} = \langle \Psi \, | \, a_i^{\dagger} a_i \, | \, \Psi \, \rangle \tag{1.1}$$

where a_i^{\dagger} (a_i) creates (annihilates) a nucleon in state i and Ψ is the many-nucleon wavefunction. In the Heisenberg picture, the equation of motion for ϱ_{ij} is then given by:

$$\dot{\varrho}_{ij} = \frac{1}{i\hbar} \langle \Psi | [a_i^{\dagger} a_j, \mathcal{H}] | \Psi \rangle = \frac{1}{i\hbar} \langle \Psi | [a_i^{\dagger}, \mathcal{H}] a_j + a_i^{\dagger} [\mathcal{H}, a_j] | \Psi \rangle$$
 (1.2)

where \mathcal{H} is the second quantized Hamiltonian:

$$\mathcal{H} = \sum_{\alpha\beta} \langle \alpha | \mathcal{T} | \beta \rangle a_{\alpha}^{\dagger} a_{\beta} + \frac{1}{2} \sum_{\substack{\alpha\beta \\ \gamma\delta}} \langle \alpha\beta | \mathcal{V} | \delta\gamma \rangle a_{\alpha}^{\dagger} a_{\beta}^{\dagger} a_{\gamma} a_{\delta}$$
 (1.3)

The kinetic and potential contributions can be calculated separately. Using the anticommutator algebra for fermionic creation and annihilation operators we have:

$$[a_{i}^{\dagger}, \mathcal{T}] = \sum_{\alpha\beta} \langle \alpha | \mathcal{T} | \beta \rangle (a_{i}^{\dagger} a_{\alpha}^{\dagger} a_{\beta} - a_{\alpha}^{\dagger} a_{\beta} a_{i}^{\dagger}) = -\sum_{\alpha} \langle \alpha | \mathcal{T} | i \rangle a_{\alpha}^{\dagger}$$
(1.4)

and its Hermitian conjugate:

$$[a_j, \mathcal{T}] = \sum_{\alpha} \langle j | \mathcal{T} | \alpha \rangle a_{\alpha}$$
 (1.5)

Thus the kinetic contribution is:

$$\begin{aligned}
\dot{\varrho}_{ij}\big|_{\text{kin.}} &= \frac{1}{i\hbar} \langle \Psi \mid \left[-\sum_{\alpha} \langle \alpha \mid \mathcal{T} \mid i \rangle a_{\alpha}^{\dagger} a_{j} + \sum_{\alpha} \langle j \mid \mathcal{T} \mid \alpha \rangle a_{i}^{\dagger} a_{\alpha} \right] \mid \Psi \rangle \\
&= \frac{1}{i\hbar} \sum_{\alpha} \left[\langle j \mid \mathcal{T} \mid \alpha \rangle \varrho_{i\alpha} - \langle \alpha \mid \mathcal{T} \mid i \rangle \varrho_{\alpha j} \right]
\end{aligned} (1.6)$$

Similarly, we have:

$$[a_{i}^{\dagger}, \mathcal{V}] = \sum_{\substack{\alpha\beta\\\gamma\delta}} \langle \alpha\beta | \mathcal{V} | \delta\gamma \rangle (a_{i}^{\dagger} a_{\alpha}^{\dagger} a_{\beta}^{\dagger} a_{\gamma} a_{\delta} - a_{\alpha}^{\dagger} a_{\beta}^{\dagger} a_{\gamma} a_{\delta} a_{i}^{\dagger})$$

$$= \sum_{\alpha\beta\gamma} [\langle \alpha\beta | \mathcal{V} | \gamma i \rangle - \langle \alpha\beta | \mathcal{V} | i\gamma \rangle] a_{\alpha}^{\dagger} a_{\beta}^{\dagger} a_{\gamma}$$
(1.7)

and its Hermitian conjugate:

$$[a_{j}, \mathcal{V}] = \sum_{\alpha\beta\gamma} [\langle j\alpha | \mathcal{V} | \gamma\beta \rangle - \langle \alpha j | \mathcal{V} | \gamma\beta \rangle] a_{\alpha}^{\dagger} a_{\beta} a_{\gamma}$$
(1.8)

Thus the potential contribution is:

$$\dot{\varrho}_{ij}\Big|_{\text{pot.}} = \frac{1}{2i\hbar} \sum_{\alpha\beta\gamma} \left[\left\langle \alpha\beta \left| \mathcal{V} \right| \gamma i \right\rangle - \left\langle \alpha\beta \left| \mathcal{V} \right| i\gamma \right\rangle \right] \left\langle \Psi \left| a_{\alpha}^{\dagger} a_{\beta}^{\dagger} a_{\gamma} a_{j} \right| \Psi \right\rangle \\
+ \frac{1}{2i\hbar} \sum_{\alpha\beta\gamma} \left[\left\langle j\alpha \left| \mathcal{V} \right| \beta\gamma \right\rangle - \left\langle \alpha j \left| \mathcal{V} \right| \beta\gamma \right\rangle \right] \left\langle \Psi \left| a_{i}^{\dagger} a_{\alpha}^{\dagger} a_{\beta} a_{\gamma} \right| \Psi \right\rangle \tag{1.9}$$

We can simplify the above expressions by noting that the only non-zero contributions to the two-particle densities will be those in which the creation operators act on the same states as the annihilation operators have acted: for the first term we must have $\alpha = \gamma$ and $\beta = j$ or $\alpha = j$ and $\beta = \gamma$; for the second we must have $i = \beta$ and $\alpha = \gamma$ or $i = \gamma$ and $\alpha = \beta$. We could further simplify it if Ψ was a Slater determinant (if

we were dealing with non-interacting nucleons in a potential well). The Hartree-Fock approximation assumes that the system wavefunction can thus be treated as a Slater determinant (which can then be used to calculate V). Thus the first two-particle density in the last equation becomes:

$$\langle \Psi | a_{\alpha}^{\dagger} a_{\beta}^{\dagger} a_{\gamma} a_{j} | \Psi \rangle = \langle \Psi | a_{\alpha}^{\dagger} a_{j} | \Psi \rangle \langle \Psi | a_{\beta}^{\dagger} a_{\gamma} | \Psi \rangle$$

$$- \langle \Psi | a_{\alpha}^{\dagger} a_{\gamma} | \Psi \rangle \langle \Psi | a_{\beta}^{\dagger} a_{j} | \Psi \rangle$$

$$= \rho_{\alpha j} \rho_{\beta \gamma} - \rho_{\alpha \gamma} \rho_{\beta j} \qquad (1.10)$$

We now introduce the single-particle Hartree-Fock potential:

$$\langle i | \mathcal{U}_{HF} | j \rangle \equiv \sum_{\alpha\beta} \left[\langle i\beta | \mathcal{V} | j\alpha \rangle - \langle i\beta | \mathcal{V} | \alpha j \rangle \right] \varrho_{\alpha\beta}$$
 (1.11)

in which case the first term in eq. 1.9 becomes, after some relabelling:

$$\frac{1}{2i\hbar} \sum_{\alpha\beta\gamma} [\langle \alpha\beta | \mathcal{V} | \gamma i \rangle - \langle \alpha\beta | \mathcal{V} | i\gamma \rangle] (\varrho_{\alpha j} \varrho_{\beta \gamma} - \varrho_{\alpha \gamma} \varrho_{\beta j})$$

$$= \frac{1}{i\hbar} \sum_{\alpha} \varrho_{\alpha j} \sum_{\beta\gamma} [\langle \alpha\beta | \mathcal{V} | \gamma i \rangle - \langle \alpha\beta | \mathcal{V} | i\gamma \rangle] \varrho_{\beta\gamma}$$

$$= -\frac{1}{i\hbar} \sum_{\alpha} \varrho_{\alpha j} \langle \alpha | \mathcal{U}_{HF} | i \rangle \tag{1.12}$$

and the second term in the same equation becomes:

$$\frac{1}{i\hbar} \sum_{\alpha} \varrho_{\alpha i} \langle j | \mathcal{U}_{HF} | \alpha \rangle \tag{1.13}$$

Thus we can rewrite the potential contribution as:

$$\dot{\varrho}_{ij}\Big|_{\text{pot.}} = \frac{1}{i\hbar} \sum_{\alpha} \left[\langle j | \mathcal{U}_{\text{HF}} | \alpha \rangle \varrho_{\alpha i} - \varrho_{j\alpha} \langle \alpha | \mathcal{U}_{\text{HF}} | i \rangle \right]$$
 (1.14)

Introducing the mean-field Hamiltonian $\mathcal{H}_{mf} = \mathcal{T} + \mathcal{U}_{HF}$ we can write the TDHF equation:

$$\dot{\varrho}_{ij} = \frac{1}{i\hbar} \sum_{\alpha} \left[\langle j | \mathcal{H}_{mf} | \alpha \rangle \varrho_{\alpha i} - \varrho_{j\alpha} \langle \alpha | \mathcal{H}_{mf} | i \rangle \right]$$
 (1.15)

We are now in a position to derive the Vlasov equation as a semi-classical approximation to TDHF. To accomplish this, we introduce the Wigner transform of the single-particle density, which has the properties of a classical phase-space density:

$$f(\mathbf{r}, \mathbf{p}) = \int \frac{\mathrm{d}s}{(2\pi\hbar)^3} \exp\left(\frac{i}{\hbar}\mathbf{p} \cdot s\right) n_{\mathbf{r}_{+}\mathbf{r}_{-}}$$
(1.16)

where we have defined $n_{r_+r_-} = \langle \Psi | a_{r_+}^{\dagger} a_{r_-} | \Psi \rangle$, $r_- = r - s/2$ and $r_+ = r + s/2$, and we have chosen the complete set of states $\{i\}$ to be the position eigenstates $\{r\}$. Alternatively, we can chose the momentum eigenstates $\{p\}$, in which case f(r,p) can be defined as:

$$f(\boldsymbol{\tau}, \boldsymbol{p}) = \int \frac{\mathrm{d}\boldsymbol{q}}{(2\pi\hbar)^3} \exp\left(-\frac{i}{\hbar}\boldsymbol{q} \cdot \boldsymbol{\tau}\right) g_{\boldsymbol{p}_{+}\boldsymbol{p}_{-}}$$
(1.17)

where we have defined $g_{p_+p_-} = \langle \Psi | a^{\dagger}_{p_+} a_{p_-} | \Psi \rangle$, $p_- = p - q/2$ and $p_+ = p + q/2$. These two definitions are completely equivalent. We can write down the equation of motion for f(r,p) from the TDHF equation as the sum of a kinetic contribution and a potential contribution which have the form:

$$\frac{\mathrm{d}f(\boldsymbol{r},\boldsymbol{p})}{\mathrm{d}t}\Big|_{\mathrm{kin.}} = \frac{1}{i\hbar} \int \frac{\mathrm{d}\boldsymbol{q}}{(2\pi\hbar)^3} \exp\left(-\frac{i}{\hbar}\boldsymbol{q}\cdot\boldsymbol{r}\right) \\
\times \int \mathrm{d}\boldsymbol{p}' \left[\langle \boldsymbol{p}_{+} | \boldsymbol{T} | \boldsymbol{p}' \rangle g_{\boldsymbol{p}'\boldsymbol{p}_{-}} - g_{\boldsymbol{p}_{+}\boldsymbol{p}'} \langle \boldsymbol{p}' | \boldsymbol{T} | \boldsymbol{p}_{-} \rangle \right] \qquad (1.18)$$

$$\frac{\mathrm{d}f(\boldsymbol{r},\boldsymbol{p})}{\mathrm{d}t}\Big|_{\mathrm{pot.}} = \frac{1}{i\hbar} \int \frac{\mathrm{d}\boldsymbol{s}}{(2\pi\hbar)^3} \exp\left(\frac{i}{\hbar}\boldsymbol{p}\cdot\boldsymbol{s}\right) \\
\times \int \mathrm{d}\boldsymbol{r}' \left[\langle \boldsymbol{r}_{+} | \mathcal{U}_{\mathrm{HF}} | \boldsymbol{r}' \rangle n_{\boldsymbol{r}'\boldsymbol{r}_{-}} - n_{\boldsymbol{r}_{+}\boldsymbol{r}'} \langle \boldsymbol{r}' | \mathcal{U}_{\mathrm{HF}} | \boldsymbol{r}_{-} \rangle \right] \qquad (1.19)$$

In the momentum representation, the kinetic energy operator the simple form $T = \hat{p}^2/2m$ and eq. 1.6 becomes (replacing the sum by an integration since we are dealing with a continuous set of states):

$$\dot{g}_{pp'} = \frac{1}{i\hbar} \int d\mathbf{q} \left[\langle \mathbf{p}' | \frac{\hat{\mathbf{p}}^2}{2m} | \mathbf{q} \rangle g_{pq} - \langle \mathbf{q} | \frac{\hat{\mathbf{p}}^2}{2m} | \mathbf{p} \rangle g_{qp'} \right]$$

$$= \frac{1}{i\hbar} \int d\mathbf{q} \left[\frac{q^2}{2m} \delta^3(\mathbf{p}' - \mathbf{q}) g_{\mathbf{p}\mathbf{q}} - \frac{p^2}{2m} \delta^3(\mathbf{q} - \mathbf{p}) g_{\mathbf{q}\mathbf{p}'} \right]$$

$$= \frac{1}{i\hbar} \left[\frac{p'^2}{2m} - \frac{p^2}{2m} \right] g_{\mathbf{p}\mathbf{p}'}$$
(1.20)

Thus the kinetic contribution becomes:

$$\frac{\mathrm{d}f(\boldsymbol{r},\boldsymbol{p})}{\mathrm{d}t}\Big|_{\mathrm{kin.}} = \frac{1}{2mi\hbar} \int \frac{\mathrm{d}\boldsymbol{q}}{(2\pi\hbar)^3} \exp\left(-\frac{i}{\hbar}\boldsymbol{q}\cdot\boldsymbol{r}\right) \\
\times \left[(\boldsymbol{p}-\boldsymbol{q}/2)^2 - (\boldsymbol{p}+\boldsymbol{q}/2)^2\right] g_{\boldsymbol{p}_{+}\boldsymbol{p}_{-}} \\
= -\frac{1}{mi\hbar} \int \frac{\mathrm{d}\boldsymbol{q}}{(2\pi\hbar)^3} \exp\left(-\frac{i}{\hbar}\boldsymbol{q}\cdot\boldsymbol{r}\right) [\boldsymbol{p}\cdot\boldsymbol{q}] g_{\boldsymbol{p}_{+}\boldsymbol{p}_{-}} \\
= -\frac{\boldsymbol{p}}{m} \cdot \nabla_{\boldsymbol{r}} \int \frac{\mathrm{d}\boldsymbol{q}}{(2\pi\hbar)^3} \exp\left(-\frac{i}{\hbar}\boldsymbol{q}\cdot\boldsymbol{r}\right) g_{\boldsymbol{p}_{+}\boldsymbol{p}_{-}} \\
= -\frac{\boldsymbol{p}}{m} \cdot \nabla_{\boldsymbol{r}} f(\boldsymbol{r},\boldsymbol{p}) \tag{1.21}$$

where we have used the fact that:

$$p \cdot \nabla_{r} \exp\left(-\frac{i}{\hbar}q \cdot r\right) = -\frac{i}{\hbar}p \cdot q \exp\left(-\frac{i}{\hbar}q \cdot r\right)$$
 (1.22)

The evaluation of the potential contribution is more cumbersome, and we need to make further assumptions: \mathcal{U}_{HF} has no momentum dependence and is local in configuration space (that is to say, it is diagonal in the position representation):

$$\langle \mathbf{r} | \mathcal{U}_{HF} | \mathbf{r}' \rangle = \mathcal{U}(\mathbf{r}) \mathcal{S}^{3}(\mathbf{r} - \mathbf{r}')$$
 (1.23)

We can thus rewrite eq. 1.14 as:

$$\dot{n}_{rr'}\Big|_{pot.} = \frac{1}{i\hbar} \int ds \left[\langle r' | \mathcal{U}_{HF} | s \rangle n_{rs} - \langle s | \mathcal{U}_{HF} | r \rangle n_{sr'} \right]
= \frac{1}{i\hbar} \left[\mathcal{U}(r') - \mathcal{U}(r) \right] n_{rr'}$$
(1.24)

Furthermore we must demand that $\mathcal{U}(r)$ is a smooth and slowly varying function of

 \boldsymbol{r} , in which case its Taylor expansion can be truncated after the first term:

$$\mathcal{U}(r+s/2) - \mathcal{U}(r-s/2) \approx s \cdot \nabla_r \mathcal{U}(r)$$
 (1.25)

Thus the potential contribution becomes:

$$\frac{\mathrm{d}f(\boldsymbol{r},\boldsymbol{p})}{\mathrm{d}t}\Big|_{\mathrm{pot.}} = \frac{1}{i\hbar} \int \frac{\mathrm{d}s}{(2\pi\hbar)^3} \exp\left(\frac{i}{\hbar}\boldsymbol{p}\cdot\boldsymbol{s}\right) \\
\times \int \mathrm{d}\boldsymbol{r}' \left[\mathcal{U}(\boldsymbol{r}-\boldsymbol{s}/2) - \mathcal{U}(\boldsymbol{r}+\boldsymbol{s}/2)\right] n_{\boldsymbol{r}_{+}\boldsymbol{r}_{-}} \\
= -\frac{1}{i\hbar} \nabla_{\boldsymbol{r}} \mathcal{U}(\boldsymbol{r}) \cdot \int \frac{\mathrm{d}s}{(2\pi\hbar)^3} \exp\left(\frac{i}{\hbar}\boldsymbol{p}\cdot\boldsymbol{s}\right) s n_{\boldsymbol{r}_{+}\boldsymbol{r}_{-}} \\
= \nabla_{\boldsymbol{r}} \mathcal{U}(\boldsymbol{r}) \cdot \nabla_{\boldsymbol{p}} \int \frac{\mathrm{d}s}{(2\pi\hbar)^3} \exp\left(\frac{i}{\hbar}\boldsymbol{p}\cdot\boldsymbol{s}\right) n_{\boldsymbol{r}_{+}\boldsymbol{r}_{-}} \\
= \nabla_{\boldsymbol{r}} \mathcal{U}(\boldsymbol{r}) \cdot \nabla_{\boldsymbol{p}} f(\boldsymbol{r},\boldsymbol{p}) \tag{1.26}$$

where we have used the same trick as for the evaluation of the kinetic contribution (eq. 1.22) except that we have taken the gradient of the kernel in the momentum space.

Combining eqs. 1.21 and 1.26 we obtain the Vlasov equation:

$$\frac{\partial f(\boldsymbol{r},\boldsymbol{p})}{\partial t} + \frac{\boldsymbol{p}}{m} \cdot \nabla_{\boldsymbol{r}} f(\boldsymbol{r},\boldsymbol{p}) - \nabla_{\boldsymbol{r}} \mathcal{U}(\boldsymbol{r}) \cdot \nabla_{\boldsymbol{p}} f(\boldsymbol{r},\boldsymbol{p}) = 0$$
 (1.27)

1.2 The collision integral

Due to nucleon-nucleon collisions, the right hand side of the Vlasov equation will no longer be 0. When a binary collision occurs, nucleons originally located at r with momenta p_1 and p_2 will scatter and emerge with new momenta p_3 and p_4 , resulting in a net change in the phase-space density at those points. If we are interested in calculating the net change in $f(r, p_1)$ we must consider two types of collisions: a) those in which a nucleon originally located between (r, p_1) and $(r + \delta r, p_1 + \delta p_1)$ is

scattered outside of that volume, resulting in a decrease of $f(\mathbf{r}, \mathbf{p}_1)$, and b) those in which a scattered nucleon ends up between $(\mathbf{r}, \mathbf{p}_1)$ and $(\mathbf{r} + \delta \mathbf{r}, \mathbf{p}_1 + \delta \mathbf{p}_1)$, resulting in an increase in $f(\mathbf{r}, \mathbf{p}_1)$.

For simplicity, we will only consider local elastic collisions in our derivation. Let $\omega(1,2;3,4)$ be the transition rate at which a nucleon located at (r,p_1) collides with a nucleon at (r,p_2) , scattering to (r,p_3) and (r,p_4) . The number $\delta n^-(r,p_1)$ of nucleons scattered outside (r,p_1) in a time interval δt is (for convenience we will write $f(r,p_i)$ as f_i and $(1-f_i)$ as $\bar{f_i}$):

$$\delta n^{-}(\mathbf{r}, \mathbf{p}_{1}) = \delta t \, \frac{\mathrm{d}\mathbf{p}_{1} \, f_{1}}{(2\pi\hbar)^{3}} \, \frac{\mathrm{d}\mathbf{p}_{2} \, f_{2}}{(2\pi\hbar)^{3}} \, \omega(1, 2; 3, 4) \, \frac{\mathrm{d}\mathbf{p}_{3} \, \bar{f}_{3}}{(2\pi\hbar)^{3}} \, \frac{\mathrm{d}\mathbf{p}_{4} \, \bar{f}_{4}}{(2\pi\hbar)^{3}}$$
(1.28)

where the vacancy factors \bar{f}_i account for the Pauli blocking of the final states. Integrating the above expression over p_2 , p_3 and p_4 we can obtain the total rate of decrease of f_1

$$\dot{f}^{-}(\mathbf{r}, \mathbf{p}_{1}) \equiv -\frac{n^{-}(\mathbf{r}, \mathbf{p}_{1})}{\delta t d\mathbf{p}_{1} / (2\pi\hbar)^{3}}
= -\frac{1}{(2\pi\hbar)^{9}} \int d\mathbf{p}_{2} d\mathbf{p}_{3} d\mathbf{p}_{4} f_{1} f_{2} \omega(1, 2; 3, 4) \bar{f}_{3} \bar{f}_{4} \qquad (1.29)$$

Similarly, the rate of increase of f_1 due to type b) collisions is:

$$\dot{f}^{+}(\mathbf{r}, \mathbf{p}_{1}) = \frac{1}{(2\pi\hbar)^{9}} \int d\mathbf{p}_{2} d\mathbf{p}_{3} d\mathbf{p}_{4} f_{3} f_{4} \omega(3, 4; 1, 2) \bar{f}_{1} \bar{f}_{2}
= \frac{1}{(2\pi\hbar)^{9}} \int d\mathbf{p}_{2} d\mathbf{p}_{3} d\mathbf{p}_{4} f_{3} f_{4} \omega(1, 2; 3, 4) \bar{f}_{1} \bar{f}_{2}$$
(1.30)

where we have used the fact that the collisions are microscopically time-reversible and therefore $\omega(3,4;1,2) = \omega(1,2;3,4)$.

We can relate the rate $\omega(1,2;3,4)$ to the differential cross-section for such colli-

sions [11]:

$$\omega(1,2;3,4) = \frac{(2\pi\hbar)^6}{m^2} \delta^3(\boldsymbol{p}_1 + \boldsymbol{p}_2 - \boldsymbol{p}_3 - \boldsymbol{p}_4) \delta(\varepsilon_1 + \varepsilon_2 - \varepsilon_3 - \varepsilon_4) \frac{\mathrm{d}\sigma(1,2;3,4)}{\mathrm{d}\Omega_{34}} \quad (1.31)$$

where the δ -functions guarantee the conservation of momenta and energy. These can be used to replace the integrations over the final momenta by an integral over the scattering angle:

$$\frac{1}{(2\pi\hbar)^6} \int d\mathbf{p}_3 d\mathbf{p}_4 \,\omega(1,2;3,4) \to v_{12} \int d\Omega_{34} \,\frac{d\sigma(1,2;3,4)}{d\Omega_{34}} \tag{1.32}$$

where v_{12} is the relative velocity of the incoming nucleons. Thus, the net rate of change of f_1 is given by:

$$\dot{f}_{1} = \dot{f}^{+}(\boldsymbol{r}, \boldsymbol{p}_{1}) + \dot{f}^{-}(\boldsymbol{r}, \boldsymbol{p}_{1})
= \frac{1}{(2\pi\hbar)^{3}} \int d\boldsymbol{p}_{2} d\Omega_{34} v_{12} \frac{d\sigma(1, 2; 3, 4)}{d\Omega_{34}} (f_{3} f_{4} \bar{f}_{1} \bar{f}_{2} - f_{1} f_{2} \bar{f}_{3} \bar{f}_{4}) \quad (1.33)$$

Combining the above equation with the Vlasov equation we get the BUU equation:

$$\dot{f}(\boldsymbol{r},\boldsymbol{p}) = \frac{\partial f(\boldsymbol{r},\boldsymbol{p})}{\partial t} + \frac{\boldsymbol{p}}{m} \cdot \nabla_{\boldsymbol{r}} f(\boldsymbol{r},\boldsymbol{p}) - \nabla_{\boldsymbol{r}} \mathcal{U}(\boldsymbol{r}) \cdot \nabla_{\boldsymbol{p}} f(\boldsymbol{r},\boldsymbol{p})
= \frac{1}{(2\pi\hbar)^3} \int d\boldsymbol{p}_2 d\Omega'_{12} v_{12} \frac{d\sigma}{d\Omega'_{12}} (f_{1'} f_{2'} \bar{f} \bar{f}_2 - f f_2 \bar{f}_{1'} \bar{f}_{2'})$$
(1.34)

where the primes denote the outgoing nucleons.

1.3 The nuclear potential

Up to now we have not specified the nature of the potential \mathcal{U} . Historically, the first potentials to be used in BUU calculations were Skyrme-type potentials, which only depend on the local density n(r). The potential energy density for the Skyrme

potentials is written as:

$$\mathcal{V}(\mathbf{r}) \equiv \mathcal{V}(n(\mathbf{r})) = \frac{A}{2}n^{2}(\mathbf{r}) + \frac{B}{\sigma + 1}n^{\sigma + 1}(\mathbf{r})$$
(1.35)

where first term is attractive and the second one repulsive. The nuclear potential associated with such an energy density is defined as the functional derivative of the latter with respect to the density:

$$\mathcal{U}(\mathbf{r}) \equiv \frac{\delta \mathcal{V}(\mathbf{r})}{\delta n(\mathbf{r})} = An(\mathbf{r}) + Bn^{\sigma}(\mathbf{r})$$
(1.36)

The three parameters A, B and σ can be determined for these potentials if we specify the ground state properties of infinite nuclear matter: the density n_o , the energy per nucleon \mathcal{B} and the nuclear compressibility coefficient κ .

To calculate the energy of a finite volume V of equilibrium nuclear matter (enclosing $\mathcal{A} = n_0 V$ nucleons), we must find a solution to the static Vlasov equation; setting the left hand side of eq. 1.27 to 0 we find:

$$\frac{p}{m} \cdot \nabla_{r} f(r, p) = \nabla_{r} \mathcal{U}(r) \cdot f(r, p)$$
 (1.37)

with the caveat the $\mathcal{U}(r)$ is not an external potential, and therefore a self-consistency condition exists: the phase-space density f(r,p) must be such that the derived configuration space density $n(r) = n_0$ generates a potential \mathcal{U} which, when we solve the stationary Vlasov equation, generates the same f(r,p) we started with. For Skyrme potentials, we can see by inspection that the required phase-space density is:

$$f(\mathbf{r}, \mathbf{p}) = \frac{g}{h^3} \Theta(\lambda - \mathcal{U}(\mathbf{r}) - p^2/2m)$$
 (1.38)

where g = 4 is the spin-isospin degeneracy factor for nuclear matter, and:

$$\mathcal{U}(r) = \begin{cases} \mathcal{U}(n_o) & \text{for } r \leq R \\ 0 & \text{for } r > R \end{cases}$$

$$\lambda = \mathcal{U}(n_o) + p_F^2/2m$$

$$\mathcal{A} = \frac{4\pi g}{3h^3} p_F^3 V$$

(The last equation is nothing but a statement of the Pauli principle). Thus the energy per nucleon of our system is:

$$\mathcal{B} = \frac{\mathcal{E}}{\mathcal{A}} = \frac{\mathcal{E}}{n_{o}V} \equiv \frac{1}{n_{o}V} \left(\int d\mathbf{r} \, d\mathbf{p} \, f(\mathbf{r}, \mathbf{p}) \, \frac{p^{2}}{2m} + \int d\mathbf{r} \, \mathcal{V}(\mathbf{r}) \right)$$
$$= \frac{3h^{2}}{10m} \left(\frac{3n_{o}}{4\pi g} \right)^{2/3} + \frac{A}{2}n_{o} + \frac{B}{\sigma + 1}n_{o}^{\sigma} \tag{1.39}$$

At equilibrium, the energy of our system must be a minimum (i.e. the pressure must be 0):

$$\mathcal{P}_{o} \equiv -\frac{\mathrm{d}\mathcal{E}}{\mathrm{d}V}\Big|_{n_{o}} = n^{2} \frac{\mathrm{d}}{\mathrm{d}n} \frac{\mathcal{E}}{V}\Big|_{n_{o}}$$

$$= \frac{h^{2}}{5m} \left(\frac{3}{4\pi g}\right)^{2/3} n_{o}^{5/3} + \frac{A}{2} n_{o}^{2} + \frac{B\sigma}{\sigma + 1} n_{o}^{\sigma + 1} = 0$$
(1.40)

Finally, the nuclear compressibility κ is:

$$\kappa \equiv 9 \frac{\mathrm{d}\mathcal{P}}{\mathrm{d}n} \bigg|_{n_o} = 9 \left[\frac{h^2}{3m} \left(\frac{3n_o}{4\pi g} \right)^{2/3} + \mathrm{A}n_o + \mathrm{B}\,\sigma\,n_o^{\sigma} \right]$$
(1.41)

Various sets of parameters A, B and σ can be found in the literature since the compressibility κ is not well known experimentally (quoted values vary from ~ 200 MeV to 350 MeV).

One of the major drawbacks of the Skyrme potentials is that they generate sharp surfaces for finite-size systems. To generate diffuse surfaces, some groups have used zero-range interactions but they add a term $\nabla^2 n(r)$ to the kinetic energy. We instead followed Bonche et al. [15] and added a Yukawa term to the potential energy density:

$$\mathcal{V}_{y}(\mathbf{r}) = \frac{V_{o}}{2} \int d\mathbf{r}' \, n(\mathbf{r}) \, n(\mathbf{r}') \, \frac{\exp{-|\mathbf{r} - \mathbf{r}'|/a}}{|\mathbf{r} - \mathbf{r}'|/a}$$
(1.42)

Note that for infinite nuclear matter, the contribution of such a term to the total energy reduces to $2\pi V_o a^3 n A$.

With the introduction of a Yukawa term (or any finite range term) in the potential, eq. 1.38 is no longer a solution of eq. 1.37 for finite-size systems (such as nuclei). In section 3.1 we present a procedure that enables us to generate self-consistent solutions of eq. 1.37 for finite-range potentials. The next refinement is to include a Coulomb term to distinguish between neutrons and protons, thus breaking the isospin degeneracy. The potential for neutrons and protons respectively becomes:

$$\mathcal{U}_{n}(\boldsymbol{r}) = An(\boldsymbol{r}) + Bn^{\sigma}(\boldsymbol{r}) + V_{o} \int d\boldsymbol{r}' n(\boldsymbol{r}') \frac{\exp{-|\boldsymbol{r} - \boldsymbol{r}'|/a}}{|\boldsymbol{r} - \boldsymbol{r}'|/a}$$

$$\mathcal{U}_{p}(\boldsymbol{r}) = \mathcal{U}_{n}(\boldsymbol{r}) + e^{2} \int d\boldsymbol{r}' n_{p}(\boldsymbol{r}') \frac{1}{|\boldsymbol{r} - \boldsymbol{r}'|}$$
(1.43)

Let us now consider the energy of nuclear matter subject to the above potential with the Coulomb potential turned off, but still distinguishing between neutrons and protons. The potential energy will simply get a contribution from the Yukawa potential:

$$\mathcal{V} = \int d\mathbf{r} \, \mathcal{V}(\mathbf{r}) = \frac{A}{2} n_o \, \mathcal{A} + \frac{B}{\sigma + 1} n_o^{\sigma} \mathcal{A} + 2\pi V_o \, a^3 \, n_o \mathcal{A}$$
 (1.44)

(We see here that the properties of nuclear matter depend on the combination (A + $4\pi V_o a^3$) and not on A, V_o and a individually). The kinetic energy on the other hand will have individual contributions from neutrons and protons:

$$T = T_{\rm n} + T_{\rm p} = \frac{3h^2}{10m} \left(\frac{3}{4\pi g}\right)^{2/3} V(n_{\rm n}^{5/3} + n_{\rm p}^{5/3})$$
 (1.45)

Introducing the asymmetry parameter $\delta \equiv (n_n - n_p)/n$, we can expand the last term in the equation to $O(\delta^2)$:

$$(n_{\rm n}^{5/3} + n_{\rm p}^{5/3}) = \left(\frac{n}{2}\right)^{5/3} \left((1+\delta)^{5/3} + (1-\delta)^{5/3}\right)$$

$$= \left(\frac{n}{2}\right)^{5/3} \left(1 + \frac{5}{3}\delta + \frac{5}{9}\delta^2 + 1 - \frac{5}{3}\delta + \frac{5}{9}\delta^2\right)$$

$$= n\left(\frac{n}{2}\right)^{2/3} \left(1 + \frac{5}{9}\delta^2\right) \tag{1.46}$$

Thus the total energy for nuclear matter at equilibrium becomes:

$$\mathcal{E} = \left(\frac{A + 4\pi V_{o} a^{3}}{2} n_{o} + \frac{B}{\sigma + 1} n_{o}^{\sigma} + \frac{3h^{2}}{10m} \left(\frac{3n_{o}}{4\pi g}\right)^{2/3}\right) \mathcal{A} + \frac{h^{2}}{6m} \left(\frac{3n_{o}}{8\pi g}\right)^{2/3} \mathcal{A} \delta^{2}$$
(1.47)

The δ^2 term is nothing but the symmetry energy. The symmetry coefficient we obtain for nuclear matter is $a_{\rm sym}=12$ MeV, which is clearly too small. To correct this problem, we must add a symmetry term to the potential energy. The simplest approach is to make the potential between unlike nucleons more attractive than between like nucleons. For computational reasons, we have chosen to modify the attractive term in the Skyrme potential energy density:

$$\frac{A}{2}n^{2} \rightarrow \frac{1}{2}(A_{l}(n_{n}^{2} + n_{p}^{2}) + 2A_{u}n_{n}n_{p})$$

$$= \frac{n^{2}}{4}((A_{l} + A_{u}) + (A_{l} - A_{u})\delta^{2}) \qquad (1.48)$$

The values of A_l and A_u must satisfy $(A_l + A_u)/2 = A$ and $A_l - A_u$ is adjusted to yield the correct symmetry energy. Thus the second potential we have used in our calculations is:

$$\mathcal{U}_{n}(\boldsymbol{r}) = A_{l}n_{n}(\boldsymbol{r}) + A_{u}n_{p}(\boldsymbol{r}) + Bn^{\sigma}(\boldsymbol{r}) + V_{o} \int d\boldsymbol{r}' \, n(\boldsymbol{r}') \frac{\exp{-|\boldsymbol{r} - \boldsymbol{r}'|/a}}{|\boldsymbol{r} - \boldsymbol{r}'|/a} \\
\mathcal{U}_{p}(\boldsymbol{r}) = A_{l}n_{p}(\boldsymbol{r}) + A_{u}n_{n}(\boldsymbol{r}) + Bn^{\sigma}(\boldsymbol{r}) + V_{o} \int d\boldsymbol{r}' \, n(\boldsymbol{r}') \frac{\exp{-|\boldsymbol{r} - \boldsymbol{r}'|/a}}{|\boldsymbol{r} - \boldsymbol{r}'|/a} \\
+ e^{2} \int d\boldsymbol{r}' \, n_{p}(\boldsymbol{r}') \frac{1}{|\boldsymbol{r} - \boldsymbol{r}'|} \tag{1.49}$$

	Eq. 1.43	Eq. 1.49	Units
A	-1567	-	MeV fm ³
A_{l-1}	-	-1313	MeV fm³
A.	-	-1856	MeV fm³
В	2806	2576	MeV fm ^{7/2}
σ	7/6	7/6	
V.	-668.7	-241.1	MeV
а	0.4598	0.5954	fm

Table 1.1: Numerical values of the parameters of potentials 1.43 and 1.49

In table 1.1 we list the parameters of potentials 1.43 and 1.49 that we have used in our work. The parameters for potential 1.43 are the same as those used in [18] and a is the same as in the original BKN parametrization [15]; a for potential 1.49 is the same as in [22]. The nuclear compressibilities associated with each one of the potentials are $\kappa = 266.6$ MeV and $\kappa = 207.5$ MeV respectively.

To see how realistic our potentials were, we generated 15 ground state nuclei (ranging from ¹²C to ²²⁸Th) using our Thomas-Fermi theory (see section 3.1) and fitted their binding energies to the liquid drop mass formula [47]:

$$\mathcal{E} = a_{\text{vol}} \mathcal{A} - a_{\text{sur}} \mathcal{A}^{2/3} - a_{\text{sym}} \left(\frac{\mathcal{N} - \mathcal{Z}}{\mathcal{A}} \right)^2 \mathcal{A} - a_{\text{coul}} \frac{\mathcal{Z}(\mathcal{Z} - 1)}{\mathcal{A}^{1/3}}$$
(1.50)

The values we obtain for the fit can be found in table 1.2, along with the experimental values. It is clear that potential 1.49 generates more realistic nuclei.

1.4 Fragmentation process

As mentioned in the introduction, the production of clusters is associated with the deexcitation of the hot, dense nuclear matter formed by the participants during a heavy ion collision. Although the process is not yet fully understood, Bertsch and

	Eq. 1.43	Eq. 1.49	Experiment
a _{vol} (MeV)	15.3	15.6	~ 16
a _{sur} (MeV)	15.4	18.7	~ 20
a _{sym} (MeV)	8.5	21.8	~ 21.4
a _{coul} (MeV)	0.67	0.71	~ 0.75

Table 1.2: Liquid drop coefficients for both potentials and the experimental values from ref. [47].

Siemens [32] proposed a simple scenario which describes qualitatively the onset of clusterization. If we assume that the hot, dense nuclear matter interacts strongly enough that thermal equilibrium is reached soon after it is formed, we can use statistical mechanics to describe and study its evolution. Using Fermi-Dirac statistics, we can calculate temperature (entropy) dependence of the total energy and pressure of the gas, thus allowing us to determine its phase-diagram. In appendix A we present an outline of the calculations involved, and in fig. 1.1 we have plotted the phase-diagram of symmetric nuclear matter for an equation of state subject only to Skyrme interactions.

As a result of a collision, the hot gas is formed at some point of the phase-diagram with average density greater than the equilibrium value and positive pressure. The gas will therefore expand (most likely adiabatically) towards equilibrium by converting internal energy into radial motion outwards. The system will continue to expand once it reaches the equilibrium point (where the pressure is 0). Depending on the separation between the initial point and the equilibrium point, the system may follow three different paths: If the separation is small, it will oscillate about the equilibrium point, expanding and contracting with very little energy loss. Such oscillations have been observed in simulations of slightly compressed or diluted nuclear matter [36], their period of oscillation agreeing remarkably well with the period of the giant monopole

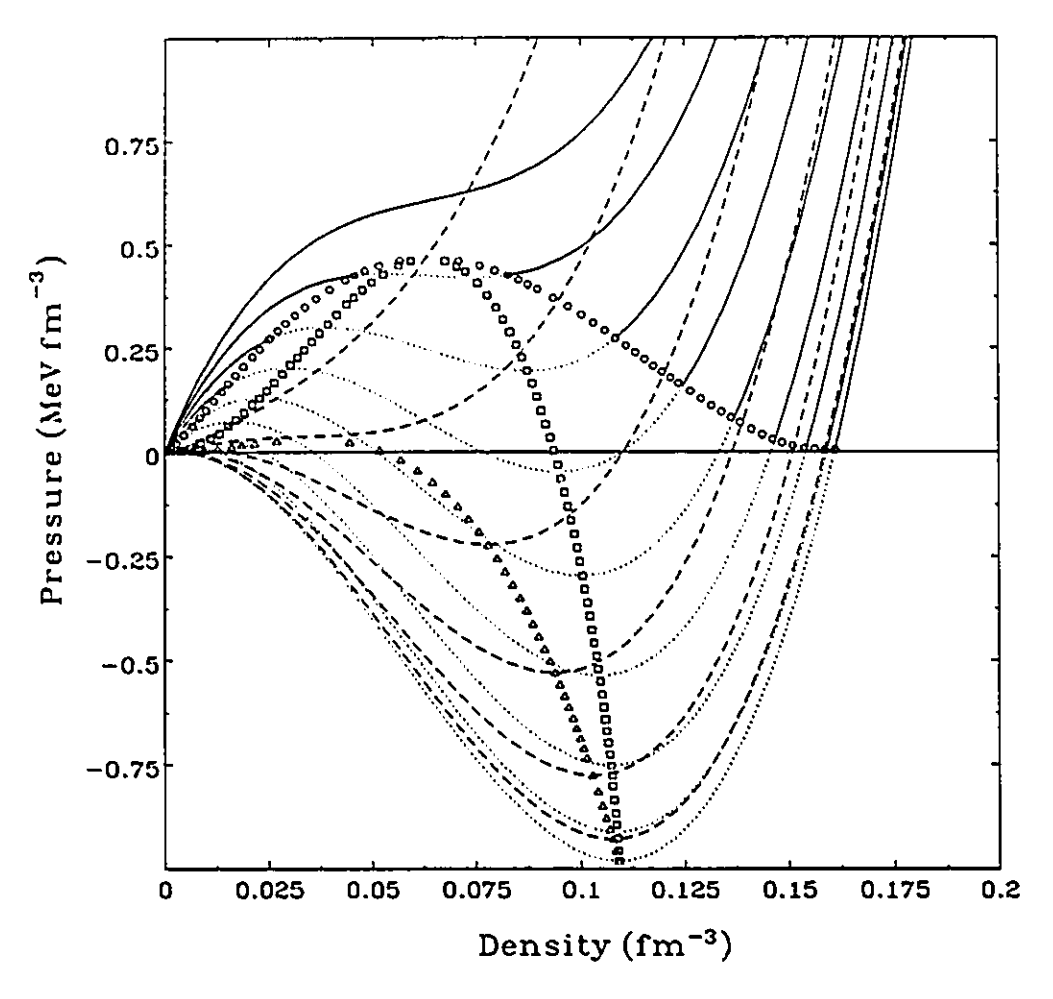


Figure 1.1: Phase diagram for nuclear matter subject to a "hard" Skyrme potential (eq. 1.36 with $A = -124/n_o$ MeV fm³, $B = 70.5/n_o^2$ MeV fm⁶ and $\sigma = 2$). We have plotted isotherms (solid and dotted lines) at 4 MeV intervals and isentropes (dashed lines) at 0.5 intervals, as well as the coexistence curve (triangles), the isothermal spinodal (circles) and the adiabatic spinodal (squares). The dotted segments of the isotherms indicate the possible coexistence of both phases of nuclear matter.

oscillations predicted by Jennings and Jackson [33]. If the distance between the initial and equilibrium points is large enough, the expansion will drive the system into the unstable region delimited by the adiabatic spinodal. Then small fluctuations in the density will no longer be dampened, and nucleation seeds will appear. If at the point at which the system crosses the adiabatic spinodal the pressure is positive, nucleation will be thermodynamically unfavourable, the seeds will evaporate and the expansion will continue until the whole system evaporates. But if the pressure at the crossing point is negative, then nucleation will be favoured, and the seeds will grow into microscopic pockets of high density (relative to the background) that will tend to attract the surrounding gas and become clusters in the later stages.

Even though this is a highly simplified description (we have assumed thermal equilibrium and that the whole system is represented by a single point in the phase diagram, thus undergoing the same evolution, whereas it is most likely that the system occupies a finite volume in the phase diagram and so the various paths compete at once), it gives us a useful understanding into the fragmentation mechanism.

Chapter 2

Numerical solution of the BUU equation

Solving the BUU equation is a non-trivial task, and we must revert to numerical methods based on Monte-Carlo sampling techniques. All numerical methods treat the left hand side on the BUU equation independently from the collision integral, under the assumption that over short time periods nucleons suffer at most one collision. Thus we assume that all collisions occurring between time t and $t + \delta t$ take place at time t, and that over the short interval δt the motion on nucleons is dictated by the Vlasov equation (eq. 1.27). In the following sections we will describe methods to solve the Vlasov equation and then how we solve the collision integral.

2.1 Test Particle Method

Let us integrate the Vlasov equation over a short time interval δt , over which the potential \mathcal{U} does not change appreciably:

$$f(\boldsymbol{r}, \boldsymbol{p}, t + \delta t) = f(\boldsymbol{r}, \boldsymbol{p}, t) - \delta t(\nabla_{\boldsymbol{p}} \mathcal{H}) \cdot (\nabla_{\boldsymbol{r}} f(\boldsymbol{r}, \boldsymbol{p}, t)) + \delta t(\nabla_{\boldsymbol{r}} \mathcal{H}) \cdot (\nabla_{\boldsymbol{p}} f(\boldsymbol{r}, \boldsymbol{p}, t))$$
(2.1)

where we have written $p/m = \nabla_p \mathcal{H}$. But the right hand side is nothing but the Taylor expansion of the phase space density about the point $(r - \delta t \nabla_p \mathcal{H}, p + \delta t \nabla_r \mathcal{H})$, thus

we get:

$$f(\mathbf{r}, \mathbf{p}, t + \delta t) = f(\mathbf{r} - \delta t \nabla_{\mathbf{p}} \mathcal{H}, \mathbf{p} + \delta t \nabla_{\mathbf{r}} \mathcal{H}, t)$$
(2.2)

which is nothing more than the equation of motion of a point particle. Thus the Test Particle Method (TPM) suggests itself naturally [34], and it has been extensively used to solve the Vlasov equation [35,36]. We substitute the smooth function f(r,p) by a large number N of point test nucleons, for which we can write the phase-space density as:

$$f_{t}(\mathbf{r}, \mathbf{p}) = C \sum_{i} \delta^{3}(\mathbf{r} - \mathbf{r}_{i}) \delta^{3}(\mathbf{p} - \mathbf{p}_{i})$$
(2.3)

where C is a normalization constant such that the integral over phase-space of the density over a small volume Ω equals the number of real nucleons A_{Ω} in that volume:

$$\mathcal{A}_{\Omega} = \int_{\Omega} d\mathbf{r} d\mathbf{p} f(\mathbf{r}, \mathbf{p}) = C \sum_{i} \int_{\Omega} d\mathbf{r} d\mathbf{p} \delta^{3}(\mathbf{r} - \mathbf{r}_{i}) \delta^{3}(\mathbf{p} - \mathbf{p}_{i}) = C N_{\Omega}$$
 (2.4)

(this is nothing but a Monte-Carlo sampling of f(r, p)). Thus $C = A/N_{\Omega} \equiv 1/N_{t}$. N_t is the number of test nucleons per real nucleon.

Taking derivatives of eq. 2.3 we have:

$$\nabla_{\boldsymbol{r}} f_{t}(\boldsymbol{r}, \boldsymbol{p}) = C \sum_{i} (\nabla_{\boldsymbol{r}} \delta^{3}(\boldsymbol{r} - \boldsymbol{r}_{i})) \delta^{3}(\boldsymbol{p} - \boldsymbol{p}_{i})$$

$$\nabla_{\boldsymbol{p}} f_{t}(\boldsymbol{r}, \boldsymbol{p}) = C \sum_{i} \delta^{3}(\boldsymbol{r} - \boldsymbol{r}_{i}) (\nabla_{\boldsymbol{p}} \delta^{3}(\boldsymbol{p} - \boldsymbol{p}_{i}))$$

$$\frac{\partial}{\partial t} f_{t}(\boldsymbol{r}, \boldsymbol{p}) = C \sum_{i} (\nabla_{\boldsymbol{r}} \delta^{3}(\boldsymbol{r} - \boldsymbol{r}_{i})) \cdot \dot{\boldsymbol{r}}_{i} \delta^{3}(\boldsymbol{p} - \boldsymbol{p}_{i}) + \delta^{3}(\boldsymbol{r} - \boldsymbol{r}_{i}) (\nabla_{\boldsymbol{p}} \delta^{3}(\boldsymbol{p} - \boldsymbol{p}_{i})) \cdot \dot{\boldsymbol{p}}_{i}$$

$$(2.5)$$

If r_i and p_i obey Hamilton's equations, $f_t(r,p)$ satisfies the Vlasov equation. The equations of motion can be solved by the leap-frog method:

$$p(t + \delta t) = p(t) - \delta t \nabla_{\mathbf{r}} \mathcal{U}(\mathbf{r}, t + \delta t/2)$$
 (2.6)

$$\mathbf{r}(t + \delta t/2) = \mathbf{r}(t - \delta t/2) + \delta t \, \mathbf{p}/m \tag{2.7}$$

To calculate the gradient of the potential at r, we need to know the density at that point. This we do by dividing the occupied configuration space into cubic cells of volume $(\delta r)^3$, and counting the number N_i of test nucleons in each cell i. The density in that cell is then:

$$n_i \approx \frac{N_i}{N_t (\delta r)^3}$$
 (2.8)

From the density we calculate the potential, and its gradient along the i^{th} direction is estimated as the half difference between the potential in the two adjacent cells along that direction. Due to the statistical nature of the Monte-Carlo sampling, even for a uniform f(r,p), $f_t(r,p)$ will not be the same in each cell i, and such fluctuations give rise to "fictitious" forces. To mitigate the problem, we assume that each test nucleon not only contributes to the cell it belongs to, but also to the six nearest neighbours, thus smoothing out the density and reducing the effect of the statistical fluctuations.

One of the major drawbacks of the TPM is that it conserves energy poorly, mostly due to the fluctuations mentioned above. For a typical cold nucleus at rest, test nucleons gain 1 to 2 MeV after 100 fmc⁻¹ of simulation. Such energy gains also result in the evaporation of nucleons from the nuclear volume: for cold ⁴⁰Ca, 1 real nucleon evaporates from the original volume after 75 fmc⁻¹, and it gets worse if we are dealing with an excited system (a cluster emerging from a collision for example). At high energies, these two drawbacks are not very important because the simulation times are usually short (less than 100 fmc⁻¹), but in the regimes we are interested in they are unacceptable, even more so if we want to study clusterization processes, since any clusters formed would eventually evaporate away.

2.2 Lattice Hamiltonian Method

Lenk and Pandharipande [12] proposed a different approach to the solution of the Vlasov equation. They considered that the configuration space lattice introduced in the TPM as a computational device to estimate the potential \mathcal{U} was a physical lattice. Then they proceeded to write down a Hamiltonian for a system of finite size test nucleons on such a lattice, and hence obtain their equations of motion. ¹

We begin by dividing configuration space into an infinite lattice of cubic cells of volume $(\delta r)^3$, each site α centered at r_{α} , in which lattice we have distributed N finite size test nucleons. The contribution of the i^{th} nucleon to the density at site α (n_{α}) is given by:

$$n_i(\boldsymbol{r}_{\alpha}) \equiv n_{\alpha i} = S(\boldsymbol{r}_{\alpha} - \boldsymbol{r}_i)$$

where $S(r_{\alpha} - r_i)$ must be continuous so that n_{α} varies smoothly as r_j changes. This is essential for exact energy conservation. Furthermore, each test nucleon must contribute to a finite number of sites. The condition that the integral (sum) of the density over the whole lattice be equal to the number \mathcal{A} of real nucleons in our system is then:

$$\mathcal{A} = (\delta r)^3 \sum_{\alpha} n_{\alpha} = (\delta r)^3 \sum_{\alpha} \sum_{i}^{N} S(\boldsymbol{r}_{\alpha} - \boldsymbol{r}_{i})$$
 (2.9)

Since A must remain constant in time we have:

$$\frac{\mathrm{d}\mathcal{A}}{\mathrm{d}t} = 0 = \frac{\partial \mathcal{A}}{\partial t} + \sum_{\beta} \frac{\partial \boldsymbol{r}_{\beta}}{\partial t} \cdot \nabla_{\boldsymbol{r}_{\beta}} \mathcal{A} + \sum_{j}^{N} \frac{\partial \boldsymbol{r}_{j}}{\partial t} \cdot \nabla_{\boldsymbol{r}_{j}} \mathcal{A}$$
$$= \sum_{j}^{N} \frac{\partial \boldsymbol{r}_{j}}{\partial t} \cdot \nabla_{\boldsymbol{r}_{j}} \left((\delta \boldsymbol{r})^{3} \sum_{\alpha} \sum_{i}^{N} S(\boldsymbol{r}_{\alpha} - \boldsymbol{r}_{i}) \right)$$

¹The following derivation can easily be extended in the case of momentum dependent fields, in which case the equation is written down for a phase-space lattice and the folding functions for the test nucleons are assumed to have finite sizes both in configuration space and in momentum space. We have written such a code, but it's implementation is prohibitively time consuming.

$$= \sum_{j}^{N} \frac{\partial \boldsymbol{r}_{j}}{\partial t} \cdot \nabla_{\boldsymbol{r}_{j}} \left((\delta r)^{3} \sum_{\alpha} S(\boldsymbol{r}_{\alpha} - \boldsymbol{r}_{j}) \right)$$
 (2.10)

where we have used the fact that the lattice is fixed in space to set $\partial r_{\alpha}/\partial t = 0$. Clearly, for the above equality to hold for all r_{α} and r_{j} we must have:

$$(\delta r)^3 \sum_{\alpha} S(\boldsymbol{r}_{\alpha} - \boldsymbol{r}_{j}) = C$$
 (2.11)

independent of r_j . C can be fixed from eq. 2.9:

$$\mathcal{A} = (\delta r)^3 \sum_{\alpha} \sum_{i}^{N} S(\boldsymbol{r}_{\alpha} - \boldsymbol{r}_{i}) = \sum_{i}^{N} (\delta r)^3 \sum_{\alpha} S(\boldsymbol{r}_{\alpha} - \boldsymbol{r}_{i}) = \sum_{i}^{N} C$$
 (2.12)

from which we get $C = A/N \equiv 1/N_t$, where N_t , as in the TPM, represents the number of test nucleons per real nucleons. Note that the above conditions are not generally satisfied by arbitrary S(r), such as Gaussians.

Once we have specified the density at every lattice site, we can calculate the potential energy density $\varepsilon(\mathbf{r}_{\alpha})$, and integrate over the lattice sites to obtain the total potential energy:

$$\mathcal{V} = (\delta r)^3 \sum_{\alpha} \varepsilon_{\alpha} \tag{2.13}$$

The Hamiltonian is then given by:

$$\mathcal{H} = \sum_{i}^{N} \frac{p_i^2}{2m} + N_t \mathcal{V}$$
 (2.14)

We are now in a position to derive the equations of motion for the test nucleons:

$$\dot{\boldsymbol{r}}_{j} = \nabla_{\boldsymbol{p}_{j}} \mathcal{H} = \frac{\boldsymbol{p}_{j}}{m}$$

$$\dot{\boldsymbol{p}}_{j} = -\nabla_{\boldsymbol{r}_{j}} \mathcal{H} = -N_{t} \nabla_{\boldsymbol{r}_{j}} \mathcal{V} = -N_{t} \sum_{\beta} \frac{\partial \mathcal{V}}{\partial n_{\beta}} \nabla_{\boldsymbol{r}_{j}} n_{\beta}$$

$$= -N_{t} \sum_{\beta} \frac{\partial}{\partial n_{\beta}} \left((\delta r)^{3} \sum_{\alpha} \epsilon_{\alpha} \right) \nabla_{\boldsymbol{r}_{j}} \sum_{i}^{N} S(\boldsymbol{r}_{\beta} - \boldsymbol{r}_{i})$$
(2.15)

$$= -N_{t}(\delta r)^{3} \sum_{\alpha\beta} \delta_{\alpha\beta} \frac{\partial \epsilon_{\alpha}}{n_{\alpha}} \sum_{i}^{N} \delta_{ij} \nabla_{\boldsymbol{r}_{i}} S(\boldsymbol{r}_{\beta} - \boldsymbol{r}_{i})$$

$$= -N_{t}(\delta r)^{3} \sum_{\beta} \mathcal{U}_{\beta} \nabla_{\boldsymbol{r}_{j}} S(\boldsymbol{r}_{\beta} - \boldsymbol{r}_{j}) \qquad (2.16)$$

where $\mathcal{U}_{\beta} = \mathcal{U}(r_{\beta})$ is the potential at site β . Since the gradients appearing in the equations of motion can be calculated analytically, the LHM is virtually free from numerical inaccuracies.

It is trivial to show that in the limit $(\delta r)^3 \to 0$ and:

$$S(\boldsymbol{r}_{\alpha} - \boldsymbol{r}_{i}) \rightarrow \frac{1}{N_{t}} \delta^{3}(\boldsymbol{r}_{\alpha} - \boldsymbol{r}_{i})$$
 (2.17)

we recover the TPM equations of motion:

$$\dot{\boldsymbol{p}}_{j} = -N_{t}(\delta r)^{3} \sum_{\beta} \mathcal{U}_{\beta} \frac{1}{N_{t}} \nabla_{\boldsymbol{r}_{j}} \delta^{3}(\boldsymbol{r}_{\beta} - \boldsymbol{r}_{j})$$

$$\rightarrow -\int d\boldsymbol{r}_{\beta} \mathcal{U}(\boldsymbol{r}_{\beta}) \nabla_{\boldsymbol{r}_{j}} \delta^{3}(\boldsymbol{r}_{\beta} - \boldsymbol{r}_{j}) = -\nabla_{\boldsymbol{r}_{j}} \mathcal{U}(\boldsymbol{r}_{j}) \qquad (2.18)$$

2.3 The cascade code

Analytical solutions of the collision integral (eq. 1.33) can not be obtained except in the most simplified scenarios, and several numerical algorithms have been proposed to solve it. One of the codes most often used is the cascade code, which we will now describe in one of it's most simple implementations [37]. We assume that during each time step, a nucleon collides with another nucleon at most once. In the energy regimes we are interested in, the only processes we need to consider are elastic collisions, and production and absorption of Δ resonances:

$$n+n \rightarrow n+n \qquad (a)$$

$$n+n \rightarrow n+\Delta \qquad (b)$$

$$n+\Delta \rightarrow n+n \qquad (c)$$

$$n+\Delta \rightarrow n+\Delta \qquad (d)$$

$$\Delta+\Delta \rightarrow \Delta+\Delta \qquad (e)$$

The cross-sections for processes (a) and (b) can be taken from fits to experimental data. We use:

$$\sigma_{\text{nn}\to\text{nn}}^{e}(\sqrt{s}) = \begin{cases} 55 & \text{if } \sqrt{s} < 1.8993\\ \frac{35}{1 + 100(\sqrt{s} - 1.8993)} + 20 & \text{if } \sqrt{s} > 1.8993 \end{cases}$$
 (2.19)

and:

$$\sigma_{\text{nn}\to\text{n}\Delta}^{i}(\sqrt{s}) = \begin{cases} 0 & \text{if } \sqrt{s} < 2.015\\ \frac{20(\sqrt{s} - 2.015)^{2}}{0.015 + (\sqrt{s} - 2.015)^{2}} & \text{if } \sqrt{s} > 2.015 \end{cases}$$
 (2.20)

(where the energies are expressed in GeV and the cross-sections in millibarns). The cross-section for process (c) can be obtained from (b) by detailed balance:

$$\sigma_{\mathbf{n}\Delta \to \mathbf{n}\mathbf{n}}^{i} = \frac{p_f^2}{8p_i^2} \sigma_{\mathbf{n}\mathbf{n} \to \mathbf{n}\Delta}^{i} \tag{2.21}$$

where the factor of 8 accounts for the spin-isospin degeneracy and the identity of the final states. The cross-sections for channels (d) and (e) are taken to be the same as for (a). The differential cross-section for the elastic channels is parametrized as:

$$\frac{\mathrm{d}\sigma}{\mathrm{d}t} = a \exp d(\sqrt{s})t(\theta) \tag{2.22}$$

where $t(\theta)$ is the momentum transfer in the center-of-mass of the colliding nucleons $(t = -2p^2(1-\cos\theta))$, and $d(\sqrt{s})$ is parametrized as:

$$d(\sqrt{s}) = \frac{6[3.65(\sqrt{s} - 1.866)]^6}{1 + [3.65(\sqrt{s} - 1.866)]^6}$$
(2.23)

The inelastic channels are assumed to scatter isotropically.

Two nucleons will collide if their distance of closest approach is less than the maximum nucleon-nucleon impact parameter:

$$b_{\text{max}} = \sqrt{\sigma_{\text{nn}}^t/\pi} \tag{2.24}$$

Since the distance of closest approach is cumbersome to calculate, a pretest is done: only if the initial separation between two nucleons is less than

$$d_{\min} = \sqrt{b_{\max}^2 + \left(ct\right)^2} \tag{2.25}$$

might the collision proceed. The nucleon-nucleon center-of-mass energy and velocity are:

$$\sqrt{s} = \sqrt{(E_1 + E_2)^2 - (p_1 + p_2)^2}$$
 (2.26)

$$\beta = \frac{p_1 + p_2}{E_1 + E_2} \tag{2.27}$$

The momentum of nucleon 1 in this frame is:

$$\mathbf{p} = \gamma \left(\frac{\mathbf{p}_1 \cdot \boldsymbol{\beta}}{\beta} - \beta E_1 \right) \frac{\boldsymbol{\beta}}{\beta} + \left(\mathbf{p}_1 - \frac{\mathbf{p}_1 \cdot \boldsymbol{\beta}}{\beta} \frac{\boldsymbol{\beta}}{\beta} \right)$$
(2.28)

and the momentum of the other one -p. Their distance in the c.m. frame is then:

$$\Delta r = (\gamma - 1) \left((r_1 - r_2) \cdot \frac{\beta}{\beta} \right) + (r_1 - r_2)$$
 (2.29)

In the time interval $-\delta t/2$ to $\delta t/2$, the two nucleons become collision candidates if:

$$\left|\frac{\Delta \boldsymbol{\tau} \cdot \boldsymbol{p}}{p}\right| < \left(\frac{p}{\sqrt{p^2 + m_1^2}} - \frac{p}{\sqrt{p^2 + m_2^2}}\right) \frac{\delta t}{2} \tag{2.30}$$

and:

$$b = \sqrt{\left(\Delta r\right)^2 - \frac{\Delta r \cdot p}{p}} < b_{\text{max}}$$
 (2.31)

Once we have a candidate pair, we must decide through which channel it will proceed. We generate a random number h between 0 and σ_{nn}^{t} , and perform the following sequence of steps:

- We compute the elastic cross-section using eq. 2.19. If h is less than the computed value, an elastic collision has occurred, and we proceed to step 4. Otherwise we proceed to the next step.
- 2. We now check for inelastic scattering:
 - i If \sqrt{s} < 2.015 GeV both particles must be nucleons and there is not enough energy to generate a Δ . We proceed to step 5.
 - ii If the masses of both particles is greater than 0.938 GeV, both are △s and no inelastic scattering can occur. Again, we proceed to step 5.
 - iii If one of the particles is a Δ , we proceed to step 3. Otherwise we compute the inelastic cross-section using eq 2.20. If h is greater than $\sigma_{nn\to nn}^e(\sqrt{s}) + \sigma_{nn\to n\Delta}^i(\sqrt{s})$, no Δ is produced and we branch to step 5. Otherwise we must now determine the mass of the excited nucleon. The parametrization we use is:

$$m_{\Delta} = \begin{cases} 1.077 + 0.75(\sqrt{s} - 2.015) & \text{for } 2.015 < \sqrt{s} < 2.220 \\ 1.231 & \text{for } \sqrt{s} > 2.220 \end{cases}$$
 (2.32)

We branch to step 4

- 3. We check for Δ absorption. We compute the cross-section from eq. 2.21. If h is greater than $\sigma_{nn\to nn}^c(\sqrt{s}) + \sigma_{n\Delta\to nn}^i(\sqrt{s})$, no inelastic scattering has occurred and we branch to step 5. Otherwise we proceed to the next step.
- 4. We now determine the final momentum p_f and the scattering angles θ_s and ϕ_s . For elastic channels we Monte-Carlo the differential cross-section using eq. 2.22 to obtain the value of t_s from which we obtain the value of θ_s . The azimuthal angle ϕ_s is randomly chosen between 0 and 2π . For inelastic channels, p_f is fixed by energy conservation, and both θ_s and ϕ_s are assumed to be isotropic.
- 5. We revert back to the original frame (either the lab frame or the c.m. of the colliding nuclei).

The initial state of the cascade code consists of two nuclei A and B approaching each other with some relative momentum p. The nucleon positions τ_i inside the nuclei are randomly assigned by Monte-Carlo sampling. Since there is no mean-field to bind the nucleons inside the nuclear volume and we want them to stay within that volume if the nucleus is isolated, no Fermi motion can be assigned to them. Then one allows the cascade to run until the number of collisions becomes sufficiently small. Because of the Monte-Carlo sampling, each run of the cascade code will generate a different final set of positions and momenta for the nucleons and we can consider each run as a simulation of a single event. Results are then averaged over many runs for each energy and impact parameter.

2.4 BUU: Cascade code plus Vlasov propagation

We now have the necessary tools to solve the BUU equation: at each time step, we use the cascade code to solve the collision integral (remember that we consider that

collisions occurring between time t and $t+\delta t$ take place simultaneously at time t) and then use the TPM or the LHM to propagate them through the mean-field. The initial state is again two nuclei approaching with relative momentum p; inside each nucleus, the test nucleons are assigned random positions. Since now there is a mean-field to keep nucleons inside the nuclear volume, we can also assign Fermi motion to them.

In coupling the cascade code to either the TPM or the LHM, we must take into consideration the fact that in the latter the system is composed of N_tA test nucleons, whereas the cascade code deals with A real nucleons. Thus we must scale the cross-sections by a factor $1/N_t$. Alternatively, one can segregate the test nucleons into N_t separate groups, with collisions only occurring between test nucleons belonging to the same group.

Having included Fermi motion in the initial state and since the Vlasov equation conserves phase-space volume (so that the Pauli principle will be respected at all times), we can now properly introduce Pauli blocking of the final states. To implement it we must calculate the phase-space density about the final positions $(r, p_{1'})$ and $(r, p_{2'})$ (see eq. 1.34). We build a sphere of radius R about r and radius P about $p_{1'}$ such that N_P test nucleons inside this volume implies complete filling. Some care must be taken when choosing N_P : if it is too small, the statistical fluctuations brought about by the Monte-Carlo sampling become important; it can not be too large since we want to sample the phase-space close to $(r, p_{1'})$. We have chosen $N_P = 8$. But specifying N_P does not determine both R and P. We add the extra condition that $R/P = R_N/p_F$ where R_N is the radius of the static nucleus and p_F is the Fermi momentum of equilibrium nuclear matter. We then define $f_{1'} = N_{1'}/(N_P - 1)$ where $N_{1'}$ is the number of test nucleons inside the phase-space volume (not counting the one at $(r, p_{1'})$), and similarly $f_{2'} = N_{2'}/(N_P - 1)$. The probability of scattering is

then $(1 - f_{1'})(1 - f_{2'})$, which we Monte-Carlo in the usual way.

2.5 Extended BUU: generating fluctuations

When we coupled the Cascade code to the Vlasov propagation, one of the features of the former was lost: the fluctuations that are intrinsic to it (both from the initial state and the scattering Monte-Carlo sampling). The scaling of the scattering cross-section (or the segregation of the N_tA test nucleons into groups) results in an averaging of fluctuations produced by the nucleon-nucleon collisions. Thus each BUU simulation can no longer be considered to represent a single event, but an average obtained over N_t events. While this is not a drawback if one is interested in flow angles or average properties, it is a serious handicap when studying clusterization processes.

The extended BUU formalism allows us to reintroduce the fluctuations in the model. In essence, we modify the Cascade code in such a way that when two test nucleons i and j collide, not only their momenta are changed by Δp , but the $2(N_t-1)$ test nucleons closest to them in phase-space also change momenta by that amount. Since N_t test nucleons represent a physical nucleon, such a collision indeed corresponds to two physical nucleons colliding. Thus fluctuations are preserved.

To determine the closest test nucleons to each i and j we need to define distance in phase-space:

$$d_{kl}^2 = (\boldsymbol{p}_k - \boldsymbol{p}_l)^2 + \left(\frac{p_F}{R_N}\right)^2 (\boldsymbol{r}_k - \boldsymbol{r}_l)^2$$
 (2.33)

where p_F is the Fermi momentum and R_N is the nuclear radius. Then the N_t closest neighbours to i change momenta by Δp and the N_t closest to j by $-\Delta p$. Of course one can choose to search only for test nucleons of the same spin-isospin species. This procedure conserves momentum, but usually not kinetic energy. With a slight

modification both can be conserved. As before, the $(N_t - 1)$ test nucleons closest to i and j are found, and their average momenta $\langle p_i \rangle$ and $\langle p_j \rangle$ calculated. Then we recalculate Δp as if the colliding nucleons had momenta $\langle p_i \rangle$ and $\langle p_j \rangle$. The test nucleons of the i set then change momenta by Δp and those of the j set by $-\Delta p$.

We also tested another procedure that was found to be faster for systems where $\mathcal{A} < N_t$. Before executing the Cascade code, the test nucleons were divided into \mathcal{A} groups as follows: starting with the test nucleon furthest from the center of mass of the system, we chose the $N_t - 1$ closest test nucleons, which were then assigned to a first physical nucleon. The furthest of the remaining unassigned test nucleons was then selected, and the $N_t - 1$ closest ones assigned to the second physical nucleon, and so on until we had \mathcal{A} physical nucleons. Then the average position and momenta of these physical nucleons were calculated, and the Cascade code executed with these physical nucleons without rescaling the cross-sections. When a collision occurred, all test nucleons belonging to the colliding physical nucleons changed momenta. Both procedures gave equivalent results, and we chose the latter for numerical speed. For systems where $\mathcal{A} > N_t$, the grouping becomes too time consuming, and we revert to the original method.

2.6 The model

We are now in a position to describe our model and list the set of parameters used. The Vlasov propagation was implemented using the LHM, while the collision part was implemented using the extended Cascade code. The numerical values for the Vlasov propagation we set to: $N_t = 100$, $\delta r = 1$ fm and $\delta t = 0.3$ fmc⁻¹. These were chosen as a compromise between accuracy and speed. As in [12], we chose the test

nucleon folding function to be:

$$S(\boldsymbol{\tau}_{\alpha} - \boldsymbol{\tau}_{i}) = \begin{cases} C(1 - \frac{|\Delta_{\alpha i}^{x}|}{b})(1 - \frac{|\Delta_{\alpha i}^{y}|}{b})(1 - \frac{|\Delta_{\alpha i}^{z}|}{b}) & \text{for } |\Delta_{\alpha i}^{u}| < b \\ 0 & \text{otherwise} \end{cases}$$
(2.34)

where $\Delta_{\alpha i}^{u} = u_{\alpha} - u_{i}$ (u being one of the cartesian components x, y or z), $C = 1/N_{t}b^{3}$ (determined by eq. 2.9) and $b = n\delta r$. In their paper, Lenk and Pandharipande argue that $n \geq 2$ for better momentum conservation in Bose systems, since the lattice breaks translational invariance, resulting in lattice friction and a net loss of momentum over extended periods of time (typically a few hundred fmc^{-1}). In our investigations with Fermi systems we set n = 1 and found that momentum was conserved to within 10^{-5} for simulations running up to 250 fm c^{-1} . The energy was conserved to within 10^{-5} .

In our simulations, we use potential 1.43. In lattice form we write it as:

$$\mathcal{U}^n_{\alpha} = \mathcal{U}^s_{\alpha} + \mathcal{U}^y_{\alpha} \tag{2.35}$$

$$\mathcal{U}^{p}_{\alpha} = \mathcal{U}^{s}_{\alpha} + \mathcal{U}^{y}_{\alpha} + \mathcal{U}^{c}_{\alpha} \tag{2.36}$$

where the n and p superscripts refer to neutrons and protons respectively and:

$$\mathcal{U}_{\alpha}^{s} = An_{\alpha} + Bn_{\alpha}^{\sigma}$$

$$\mathcal{U}_{\alpha}^{v} = V_{o}(\delta r)^{3} \sum_{\beta} \frac{\exp|\mathbf{r}_{\alpha} - \mathbf{r}_{\beta}|/a}{|\mathbf{r}_{\alpha} - \mathbf{r}_{\beta}|/a} n_{\beta}$$

$$\mathcal{U}_{\alpha}^{c} = e^{2}(\delta r)^{3} \sum_{\beta} \frac{1}{|\mathbf{r}_{\alpha} - \mathbf{r}_{\beta}|} n_{\beta}^{v}$$

Calculating $\mathcal{U}^{\nu}_{\alpha}$ and \mathcal{U}^{c}_{α} as written is very time consuming, and we instead solve the associated differential equations

$$\nabla_{\mathbf{r}}^{2} \mathcal{U}_{\alpha}^{y} - \frac{1}{a^{2}} \mathcal{U}_{\alpha}^{y} = -4\pi a \nabla_{\mathbf{o}} n_{\alpha} \quad , \quad \nabla_{\mathbf{r}}^{2} \mathcal{U}_{\alpha}^{c} = -4\pi e^{2} n_{\alpha}^{p}$$
 (2.37)

by a relaxation method with Gauss' accelerators [38,39]. Given that the lattice densities are slowly varying functions of time, if one starts with the known potentials at time t, the new solutions at time $t + \delta t$ converge after 3 iterations of the method.

The cascade code was implemented using the method described in sec. 2.5. Because the number of nucleons involved was small (20 Ne+ 20 Ne), we chose the grouping method. Since the beam energies we studied were low (45 MeV beam), two simplifications were possible: the inelastic cross-sections being almost negligible, the inelastic channels were left out of the code; also, the differential cross-section for the elastic channels (eq. 2.22) was taken to be constant (i.e., isotropic scattering).

The initial distribution of test nucleons inside the nucleus was done with particular care to try to obtain as cold a nucleus as possible. From the density profiles obtained by our Thomas-Fermi solutions (see sec. 3.1), we computed n_{α}^{TF} , the density at each lattice site. We then assigned a tentative position to the i^{th} test nucleon, and calculated its contribution to the density at each lattice site $(n_{\alpha i})$. If for any one of the sites to which it contributed,

$$n_{\alpha i} + \sum_{j=1}^{i-1} n_{\alpha j} \ge (1 + \epsilon) n_{\alpha}^{\text{TF}}$$
 (2.38)

(where ϵ is a tolerance factor), then the position was rejected and the procedure restarted; otherwise we proceeded with the next test nucleon. Depending on the value of ϵ , the average number of trials needed to accommodate a test nucleon varied quite significantly: for $\epsilon = 0.1$, 50 trials were necessary; for $\epsilon = 0.01$, 10^6 trials. In our simulations, we set $\epsilon = 0.025$, for which $\sim 10^4$ trials were needed. Once we had calculated n_{α} , we calculated the corresponding Fermi momentum at each site and assigned momenta to each test nucleon again by Monte-Carlo sampling.

The nuclei thus constructed were then boosted with the appropriate momenta

and impact parameter. Because of the low energies and the finite-range terms of the potential, the simulations were run up to 200 fmc⁻¹ after the first nucleon-nucleon collision. This required an average of 16 hours of CPU on a dedicated VaX 785-11.

2.7 Testing our model

As a test for our extended BUU code we simulated an experiment done at the National Superconducting Cyclotron Laboratory in Michigan State University (MSU) in which the reaction studied was 20 Ne on NaF at 45 MeV per nucleon. The main components of the detector were a forward charge detector, Luilt at Chalk River Laboratories, the MSU 4π array (plastic ball) and a silicon telescope. The forward array measured the total charge Z of particles emerging in the forward direction between 2.5° and 17°, with an energy threshold of 15 MeV per nucleon. The 4π array measured particles emerging at angles between 19° and 161°, with an energy threshold of 17 MeV per nucleon, and was mainly used to tag the multiplicity M (number of charged particles) of each event. The silicon telescope was located at an angle of 47° . For further details on the experiment, see [19,20,40].

The data we were interested in were: a) the inclusive spectra of Z=1 clusters; b) the forward charge Z versus multiplicity M. At the time of our analysis, the experimental spectra available were: i) integrated over the whole angular range of the plastic ball, ii) integrated over smaller angular ranges, iii) with a multiplicity tag from the plastic ball.

In order to be able to compare the results of our simulations with the data, we had to identify the clusters resulting from each event and to determine their particle content (mass and charge), their energy and angle of emergence, which then would allow us to determine the charge in the forward direction and the multiplicity

in the plastic ball. But BUU type models produce density distributions in which pockets of significant local density can be identified against a diffuse background, and a cluster searching algorithm had to be devised with the requirement that the clusters produced have an integral mass and charge. This we achieved by the following two step procedure. First, a coarse-grained scan in which preliminary clusters were identified: we assigned test nucleons to a preliminary cluster if its configuration space distance to any test nucleon already in the cluster was less than a certain value γ (obviously, setting γ equal to a small number corresponds to scanning for very high density pockets and setting it to a large number corresponds to scanning for very diffuse clusters). Of the clusters thus obtained, only those whose mass was greater than 0.5 physical nucleons were retained, the others being dismissed and their test nucleons assigned to the background. The second step was to complete the retained clusters so that they had integral mass and charge: for each preliminary cluster, the test nucleons in the background were ordered according to their phase-space distance to the center of mass of the cluster, and as many of the closest test nucleons were assigned to the cluster as were necessary to have integral charge and mass. After "completing" all clusters, any test nucleons still in the background were considered to be free nucleons. Note that since all preliminary clusters retained have some neutron and some proton content, the smallest cluster produced by our algorithm had A=2.

In order to determine an optimal γ , we looked at the number of clusters predicted as a function of γ , and found that there is a critical value beyond which the number of clusters (as well as their mass distribution) quickly saturates. We chose $\gamma = 0.225$ fm, which corresponds to twice the test nucleon radius if we assume that the volume it occupies is N_t times smaller than the physical nucleon volume. Doubling the value

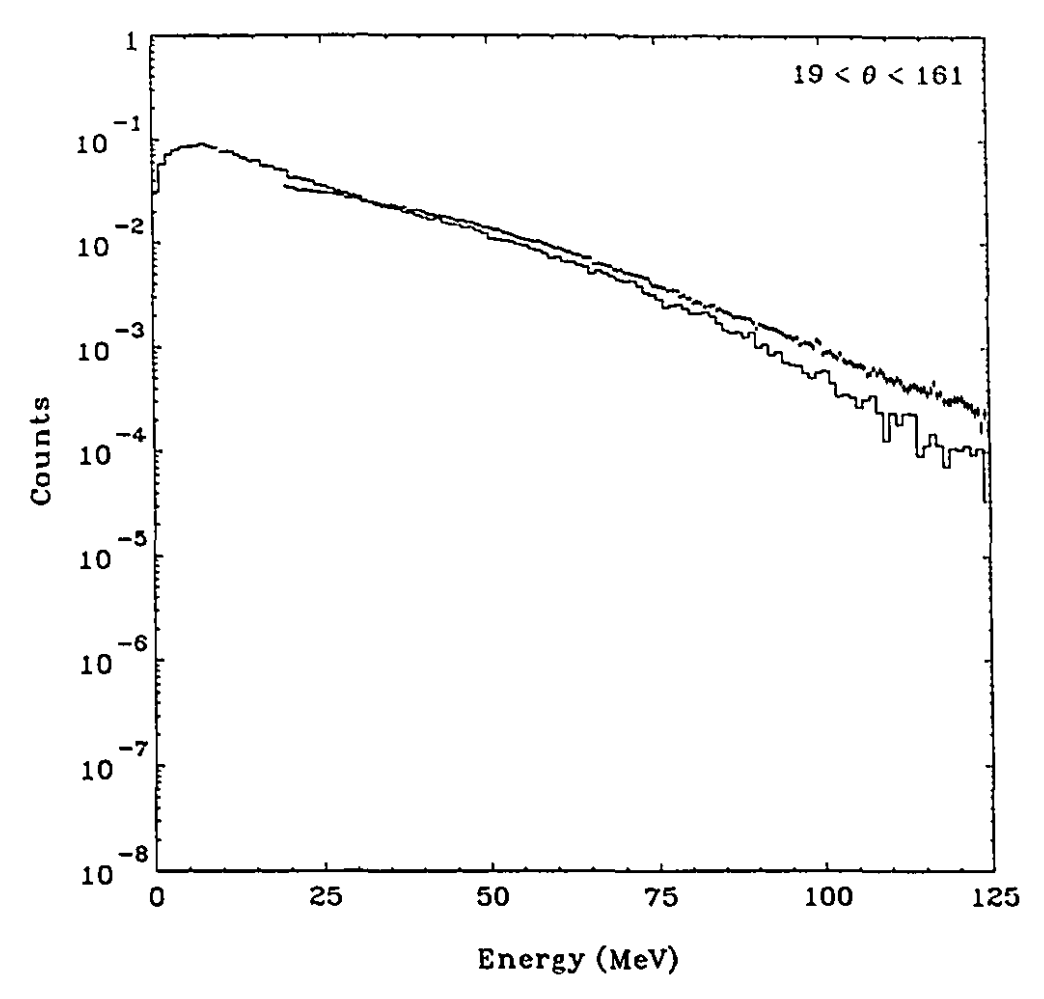


Figure 2.1: Inclusive distribution over energy of Z=1 particles, integrated over the whole plastic ball polar angle coverage. The data are the dots with the error bars and the calculation is the histogram. The latter has been normalized to the data.

of γ only changed our results by less than 10%. For this value of γ the average density of the predicted clusters was one third of the equilibrium nuclear matter density.

Using our model, we simulated 750 events spanning an impact parameter range from 0 to 6 fm. The statistics generated were adequate for high cross-section events. To use the Si telescope data we would have needed much higher statistics. When analyzing the inclusive spectra for $\mathcal{Z}=1$ we normalized the theoretical cross-sections to their experimental counterparts (total cross-sections have not been a problem in BUU calculations).

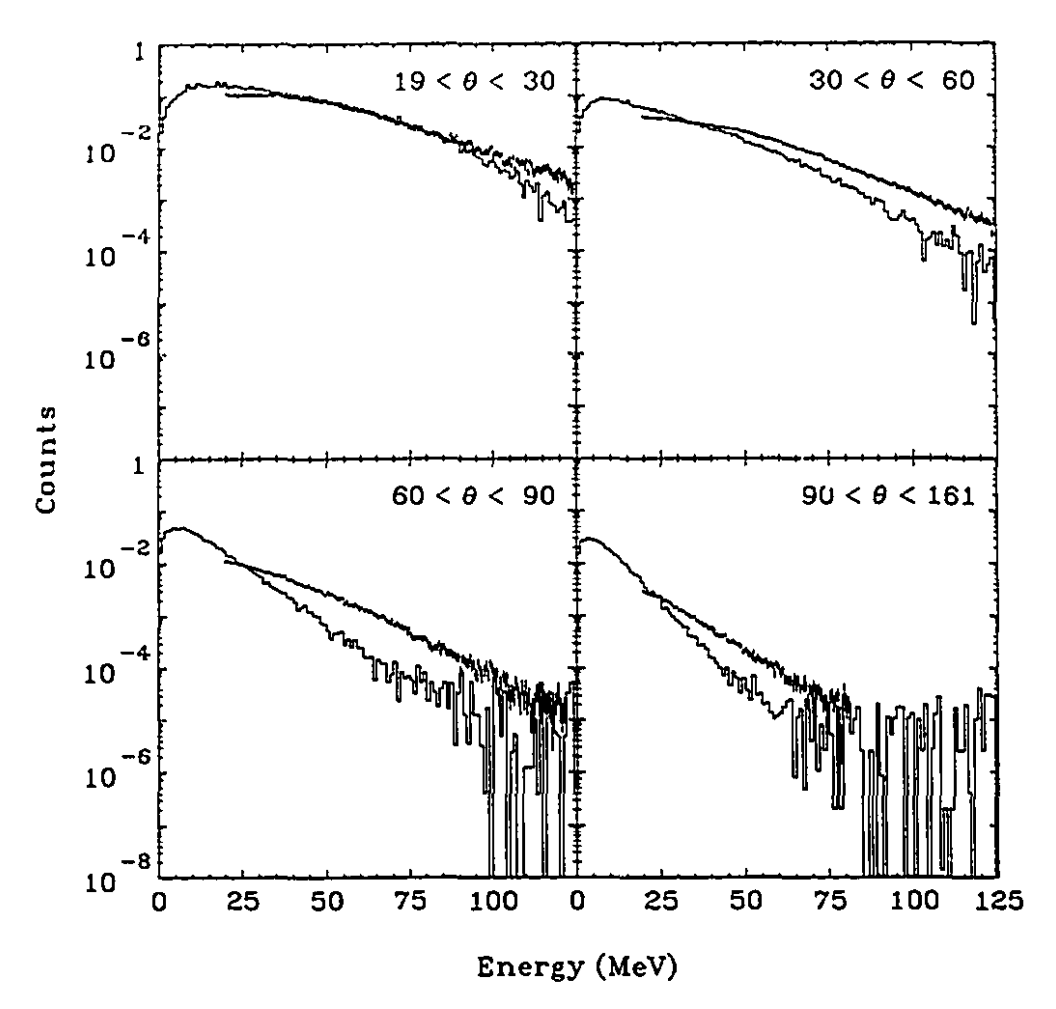


Figure 2.2: As in Fig. 2.1, but for smaller angular ranges. The normalization is the same one used for the full angle distributions.

In fig. 2.1 we plot dN/dE for our calculation and the experiment, integrated over the full angular coverage of the plastic ball, and the agreement is quite reasonable. Fig. 2.2 gives more details, separating inclusive distributions into different angular bins. When the cross-sections are large, theory and experiment agree quite well, but there are discrepancies at backward angles where the cross-sections are small.

Fig. 2.3 presents more exclusive data where inclusive cross-sections are shown for fixed plastic ball multiplicities; of the cases displayed, M=5 represents the most central collisions. We find that the calculation reproduces these very well. For brevity M=1 data and calculations are not shown in that figure, although the agreement

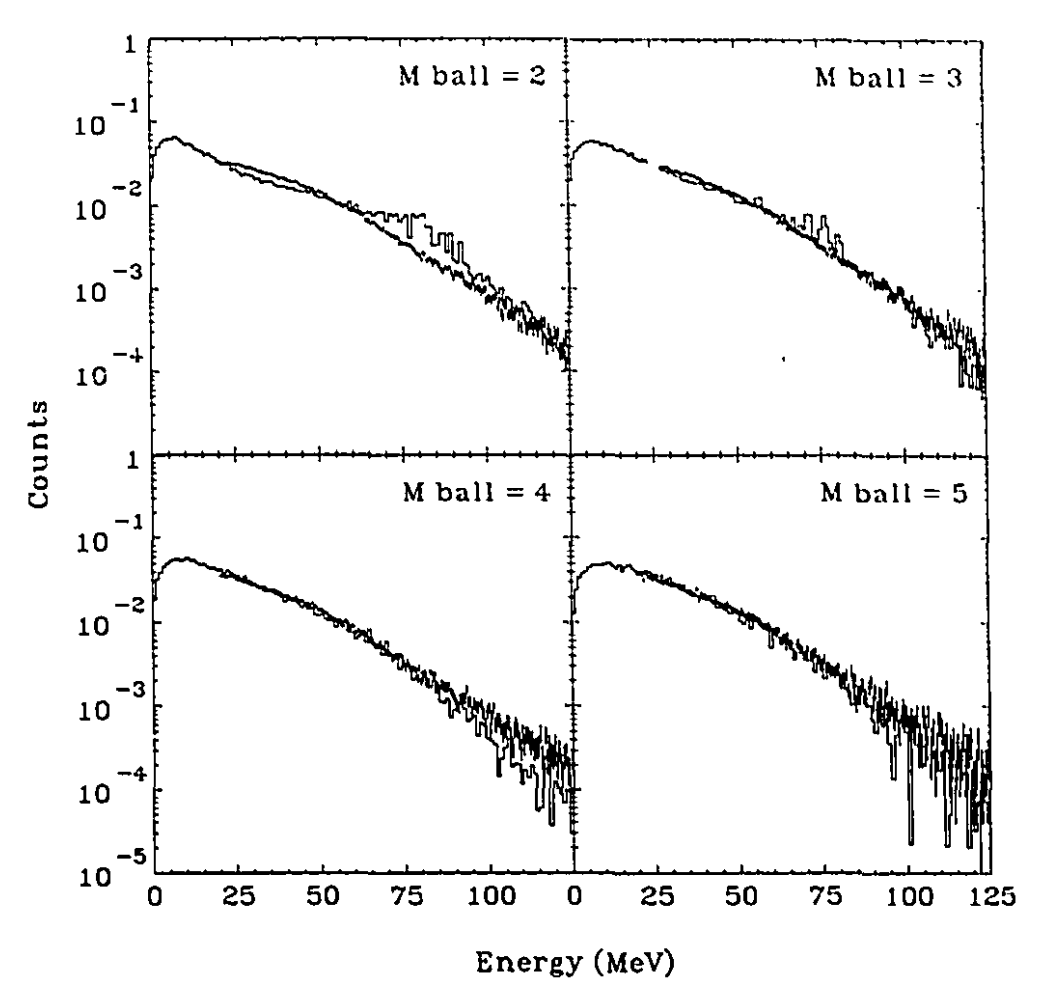


Figure 2.3: Inclusive distributions over energy of $\mathcal{Z}=1$ particles for events with a specific plastic ball multiplicity. The solid dots with error bars represent the data and the histogram the calculation.

was of similar quality.

In the energy regime of this experiment, an important question often addressed is the relationship between charge multiplicity and impact parameter b. On the basis of the participant/spectator model presented in the introduction and on results from experiments at higher energy regimes, we expect that a high charge multiplicity in the plastic ball (accompanied by a low total charge in the forward array) would be the signature of a near-central collision. On the other hand, a low charge multiplicity in the plastic ball (accompanied by a high total charge in the forward array) would

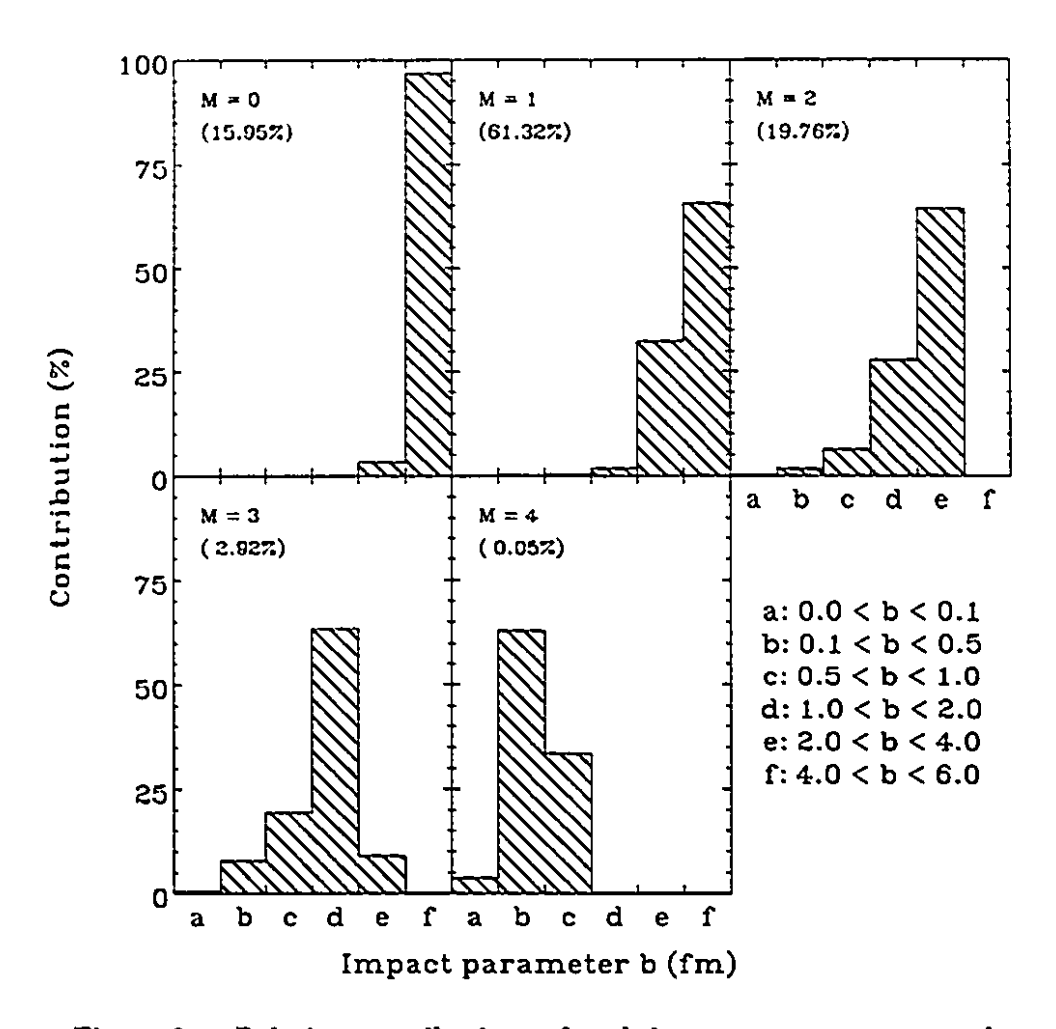


Figure 2.4: Relative contributions of each impact parameter to each individual plastic ball multiplicity M. The number in parentheses gives the relative probability of a given multiplicity.

be the signature of a peripheral collision. In fig. 2.4 we show the results from our calculation. In it we have depicted the relative contributions of different impact parameter ranges for a given plastic ball multiplicity M. The numbers in parentheses give the relative probabilities of the corresponding multiplicity (relative to the total number of events). While there is no experimental data to compare our results with, we find such detailed analysis helps to highlight the impact parameter-multiplicity relationship.

In fig. 2.5 we show a plot of the ball multiplicity M versus average total charge Z in

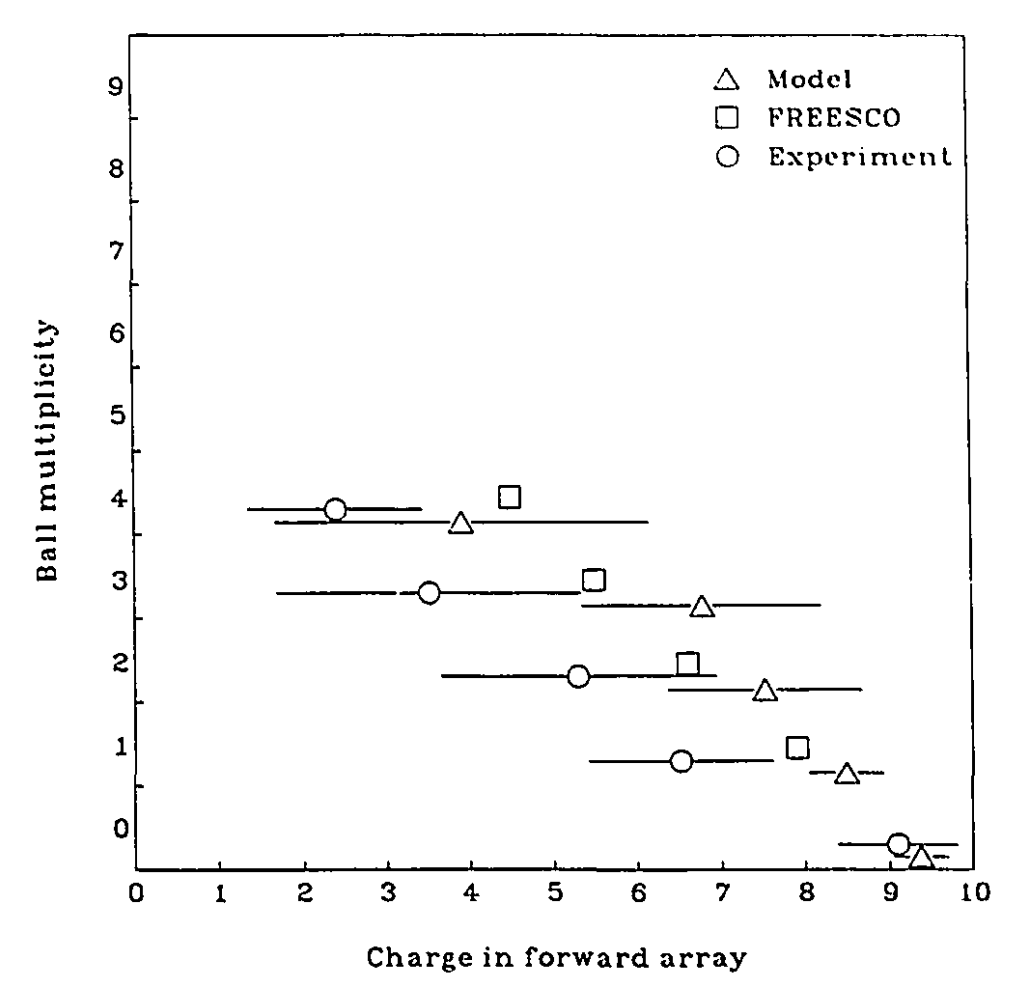


Figure 2.5: For a given ball multiplicity M, the average total charge Z in the forward array is shown. For clarity, the different symbols have been offset slightly in the vertical direction (from top to bottom they correspond to M = 4, 3, 2, 1, 0.)

the forward array. The error bars on the theoretical points are of a statistical nature. This plot suggests that our connection between multiplicity and impact parameter is quite reasonable. The trend of the calculation follows that of the experimental data, with only one bin where there is no overlap between the theoretical results and the data. Also for comparison we have included results from FREESCO simulations [41]. Thus our intuitive picture is supported by our results.

Chapter 3

Thomas-Fermi theory

3.1 Thomas-Fermi theory for static nuclei

In section 1.3 we mentioned that as a result of the introduction of a Yukawa term in the nuclear potential, the phase-space density defined in eq. 1.38 is no longer a solution of the static Vlasov equation. We must devise a more general and systematic approach that will allow us to calculate f(r,p) for a wide range of nuclear potentials. The starting point will be the Thomas-Fermi (TF) theory, since it can be regarded as a semi-classical approximation to the Hartree-Fock theory, just as the Vlasov equation is a semi-classical approximation to TDHF. Our objective is to obtain TF solutions with specified angular momentum, but we must start from TF solutions with no angular momentum.

3.1.1 Derivation of the Thomas-Fermi equations for nuclei

Our goal is to find a phase-space distribution f(r, p) which will minimize the energy of our system, in this case a nucleus composed of A nucleons and for the moment symmetric ($\mathcal{Z} = \mathcal{N}$) with no Coulomb interaction between the protons. We can then

write down the (non-relativistic) energy of such system as:

$$\mathcal{E} = \int d\mathbf{r} d\mathbf{p} f(\mathbf{r}, \mathbf{p}) \frac{p^2}{2m} + \int d\mathbf{r} \, \mathcal{V}(\mathbf{r})$$
 (3.1)

where V(r) is the potential energy density at r. In turn, we write the number of nucleons A as:

$$A = \int d\mathbf{r} d\mathbf{p} f(\mathbf{r}, \mathbf{p}) \equiv \int d\mathbf{r} n(\mathbf{r})$$
 (3.2)

Thus, we want to minimize eq. 3.1 with the constraint imposed by eq. 3.2. Using Lagrange multipliers we can then do an unconstrained minimization of the quantity:

$$\mathcal{E}' = \int d\mathbf{r} d\mathbf{p} f(\mathbf{r}, \mathbf{p}) \frac{p^2}{2m} + \int d\mathbf{r} \, \mathcal{V}(\mathbf{r}) + \lambda \left(\mathcal{A} - \int d\mathbf{r} \, n(\mathbf{r}) \right)$$
(3.3)

Since the potential energy density is independent of p, we can make the ansatz that at every point r, the momentum distribution will be a filled Fermi sphere (which guarantees that the kinetic energy at that point will be a minimum):

$$f(\mathbf{r}, \mathbf{p}) = \frac{g}{h^3} \Theta(p_{\mathbf{F}}(\mathbf{r}) - p)$$
 (3.4)

where g is the spin-isospin degeneracy (4 for symmetric potentials and 2 otherwise). We can readily calculate the density at r:

$$n(\mathbf{r}) \equiv \int \mathrm{d}\mathbf{p} \, f(\mathbf{r}, \mathbf{p}) = \frac{g}{h^3} \int \mathrm{d}\mathbf{p} \, \Theta(p_{\mathrm{F}}(\mathbf{r}) - p) = \frac{4\pi g}{3h^3} p_{\mathrm{F}}(\mathbf{r})^3 \tag{3.5}$$

(Note that this satisfies the Pauli exclusion principle).

Performing the momentum space integration of eq. 3.3 we get:

$$\mathcal{E}' = \int d\mathbf{r} \left[\frac{4\pi g}{10m} p_{\mathbf{F}}(\mathbf{r})^5 + \mathcal{V}(\mathbf{r}) - \lambda n(\mathbf{r}) \right] + \lambda \mathcal{A}$$

$$= \int d\mathbf{r} \left[\frac{3h^2}{10m} \left(\frac{3}{4\pi g} \right)^{2/3} n(\mathbf{r})^{5/3} + \mathcal{V}(\mathbf{r}) - \lambda n(\mathbf{r}) \right] + \lambda \mathcal{A} \qquad (3.6)$$

Under the variation $n(r) \rightarrow n(r) + \delta n(r)$, the first order change in \mathcal{E}' becomes:

$$\delta \mathcal{E}' = \int d\mathbf{r} \left[\frac{h^2}{2m} \left(\frac{3n(\mathbf{r})}{4\pi g} \right)^{2/3} + \mathcal{U}(\mathbf{r}) - \lambda \right] \delta n(\mathbf{r})$$
 (3.7)

(remember that the potential $\mathcal{U}(\mathbf{r})$ is the functional derivative of the potential energy density with respect to $n(\mathbf{r})$). Since $\delta n(\mathbf{r})$ is an arbitrary function, the above equation will only be 0 if the term in square brackets is identically 0 for all \mathbf{r} :

$$\frac{h^2}{2m} \left(\frac{3n(\mathbf{r})}{4\pi g} \right)^{2/3} + \mathcal{U}(\mathbf{r}) - \lambda = 0 \tag{3.8}$$

We can now easily prove that if n(r) satisfies the previous equation, it will also be a static solution of the Vlasov equation (eq. 1.27). With our ansatz for f(r, p), the Vlasov equation becomes:

$$\frac{\partial f(\boldsymbol{r},\boldsymbol{p})}{\partial t} = -\frac{p}{m} \cdot \nabla_{\boldsymbol{r}} f(\boldsymbol{r},\boldsymbol{p}) + \nabla_{\boldsymbol{r}} \mathcal{U}(\boldsymbol{r}) \cdot \nabla_{\boldsymbol{p}} f(\boldsymbol{r},\boldsymbol{p})
= -\frac{p}{m} \cdot \nabla_{\boldsymbol{r}} \frac{g}{h^{3}} \Theta(p_{F}(\boldsymbol{r}) - p) + \nabla_{\boldsymbol{r}} \mathcal{U}(\boldsymbol{r}) \cdot \nabla_{\boldsymbol{p}} \frac{g}{h^{3}} \Theta(p_{F}(\boldsymbol{r}) - p)
= \frac{g}{h^{3}} \left[-\frac{p}{m} \delta(p_{F}(\boldsymbol{r}) - p) \nabla_{\boldsymbol{r}} p_{F}(\boldsymbol{r}) - \nabla_{\boldsymbol{r}} \mathcal{U}(\boldsymbol{r}) \delta(p_{F}(\boldsymbol{r}) - p) \right] \cdot \hat{\boldsymbol{p}}
= \frac{g}{h^{3}} \delta(p_{F}(\boldsymbol{r}) - p) \left[-\frac{p}{m} \nabla_{\boldsymbol{r}} p_{F}(\boldsymbol{r}) - \nabla_{\boldsymbol{r}} \mathcal{U}(\boldsymbol{r}) \right] \cdot \hat{\boldsymbol{p}} \tag{3.9}$$

But since f(r, p) is a solution of eq. 3.8, we have:

$$\nabla_{\boldsymbol{r}} \mathcal{U}(\boldsymbol{r}) = \nabla_{\boldsymbol{r}} \left[\lambda - \frac{h^2}{2m} \left(\frac{3n(\boldsymbol{r})}{4\pi g} \right)^{2/3} \right] = -\left(\frac{3}{4\pi g} \right)^{2/3} \frac{2}{3} n(\boldsymbol{r})^{-1/3} \nabla_{\boldsymbol{r}} n(\boldsymbol{r})$$
(3.10)

Furthermore, from eq. 3.5:

$$\nabla_{\mathbf{r}} p_{\mathbf{F}}(\mathbf{r}) = \nabla_{\mathbf{r}} \left(\frac{3h^3 n(\mathbf{r})}{4\pi g} \right)^{1/3} = \left(\frac{3h^3}{4\pi g} \right)^{1/3} \frac{1}{3} n(\mathbf{r})^{-2/3} \nabla_{\mathbf{r}} n(\mathbf{r})$$
(3.11)

Because of the $\delta(p_F(r) - p)$ term, eq. 3.9 will automatically be 0 for $p \neq p_F(r)$; and for $p = p_F(r)$ we can use the last two equations:

$$\frac{\partial f(\mathbf{r}, \mathbf{p})}{\partial t} = \frac{g}{h^3} \left[-\frac{1}{3m} \left(\frac{3h^3}{4\pi g} \right)^{2/3} n(\mathbf{r})^{1/3} n(\mathbf{r})^{-2/3} \right]$$

+
$$\frac{h^2}{3m} \left(\frac{3}{4\pi g} \right)^{2/3} n(\mathbf{r})^{-1/3} \right] \nabla_{\mathbf{r}} n(\mathbf{r}) \cdot \hat{\mathbf{p}} = 0$$
 (3.12)

In the more general case of non-symmetric nuclei or if we include the Coulomb interaction, the derivation is much the same, except that the constraint on A is now replaced by:

$$\int d\mathbf{r} \, n_{\rm n}(\mathbf{r}) = \mathcal{N} \quad , \qquad \int d\mathbf{r} \, n_{\rm p}(\mathbf{r}) \mathcal{Z} \tag{3.13}$$

with the corresponding Lagrange multipliers λ_n and λ_p . The steps are the same as for the symmetric case (eqs. 3.1-3.8), leading to the two coupled equations:

$$\frac{h^2}{2m} \left(\frac{3n_n(\boldsymbol{r})}{4\pi g} \right)^{2/3} + \mathcal{U}_n(\boldsymbol{r}) - \lambda_n = 0 \tag{3.14}$$

$$\frac{h^2}{2m} \left(\frac{3n_p(\boldsymbol{r})}{4\pi g} \right)^{2/3} + \mathcal{U}_p(\boldsymbol{r}) - \lambda_p = 0 \tag{3.15}$$

where of course, g is now 2.

3.1.2 Implementation of the Thomas-Fermi equation

To solve eq. 3.8 (or eqs. 3.14 and 3.15) we use an iterative procedure. Starting from an initial density profile (either a Myers distribution [43], which had been previously used in heavy ion calculations [44], or a uniform sphere) and a guessed value for λ , we proceed as follows:

- 1. From the current density profile, we calculate the finite range components of the potential (the Yukawa term and, for protons, the Coulomb term).
- 2. Using the current value of λ , we use eq. 3.8 to calculate the density $n(\tau)$ at every point τ .

- 3. We integrate the density profile n(r) to obtain the total number of nucleons and compare it to A, modifying λ and loop back to the previous step until both numbers agree within the prescribed accuracy.
- 4. Loop back to step 1 until two successive iterations give the same λ .

The numerical implementation of the above procedure is rather simple, and the only problem is the calculation of the Coulomb and Yukawa terms in the nuclear potential. Since eq. 3.8 (or eqs. 3.14 and 3.15 in the non-symmetric case) is spherically symmetric, we expect n(r) (or $n_n(r)$ and $n_p(r)$) also to be spherically symmetric. In that case, we can write the Coulomb term as:

$$\mathcal{U}_{c}(\mathbf{r}) = e^{2} \int d\mathbf{r}' \, n_{p}(\mathbf{r}') \frac{1}{|\mathbf{r} - \mathbf{r}'|} \\
= 4\pi e^{2} \sum_{lm} \sqrt{4\pi} Y_{lm}(\theta, \phi) \int d\Omega' \, Y_{00}(\theta', \phi') Y_{lm}^{*}(\theta', \phi') \int_{0}^{\infty} d\mathbf{r}' \, r'^{2} \frac{r_{<}^{l}}{r_{>}^{l+1}} \, n_{p}(r') \\
= 4\pi e^{2} \int_{0}^{\infty} d\mathbf{r}' \, r'^{2} \frac{1}{r_{>}} \, n_{p}(r') \\
= 4\pi e^{2} \left[\frac{1}{r} \int_{0}^{r} d\mathbf{r}' \, r'^{2} \, n_{p}(r') + \int_{r}^{\infty} d\mathbf{r}' \, r' \, n_{p}(r') \right] \tag{3.16}$$

where we have expanded $\frac{1}{|\mathbf{r} - \mathbf{r}'|}$ in terms of spherical harmonics ([42], page 102) and used their orthonormality to perform the angular integration. Similarly, the Yukawa term can be written as:

$$\mathcal{U}_{y}(\mathbf{r}) = V_{o} \int d\mathbf{r}' n(\mathbf{r}) \frac{\exp{-|\mathbf{r} - \mathbf{r}'|/a}}{|\mathbf{r} - \mathbf{r}'|/a}
= -4\pi V_{o} \sum_{lm} \sqrt{4\pi} \int d\Omega' Y_{00}(\theta', \phi') Y_{lm}^{**}(\theta', \phi')
\int_{0}^{\infty} dr' r'^{2} j_{l}(ir_{<}/a) h_{l}(ir_{>}/a) n(r')
= -4\pi V_{o} \int_{0}^{\infty} dr' r'^{2} j_{0}(ir_{<}/a) h_{0}(ir_{>}/a) n(r')$$

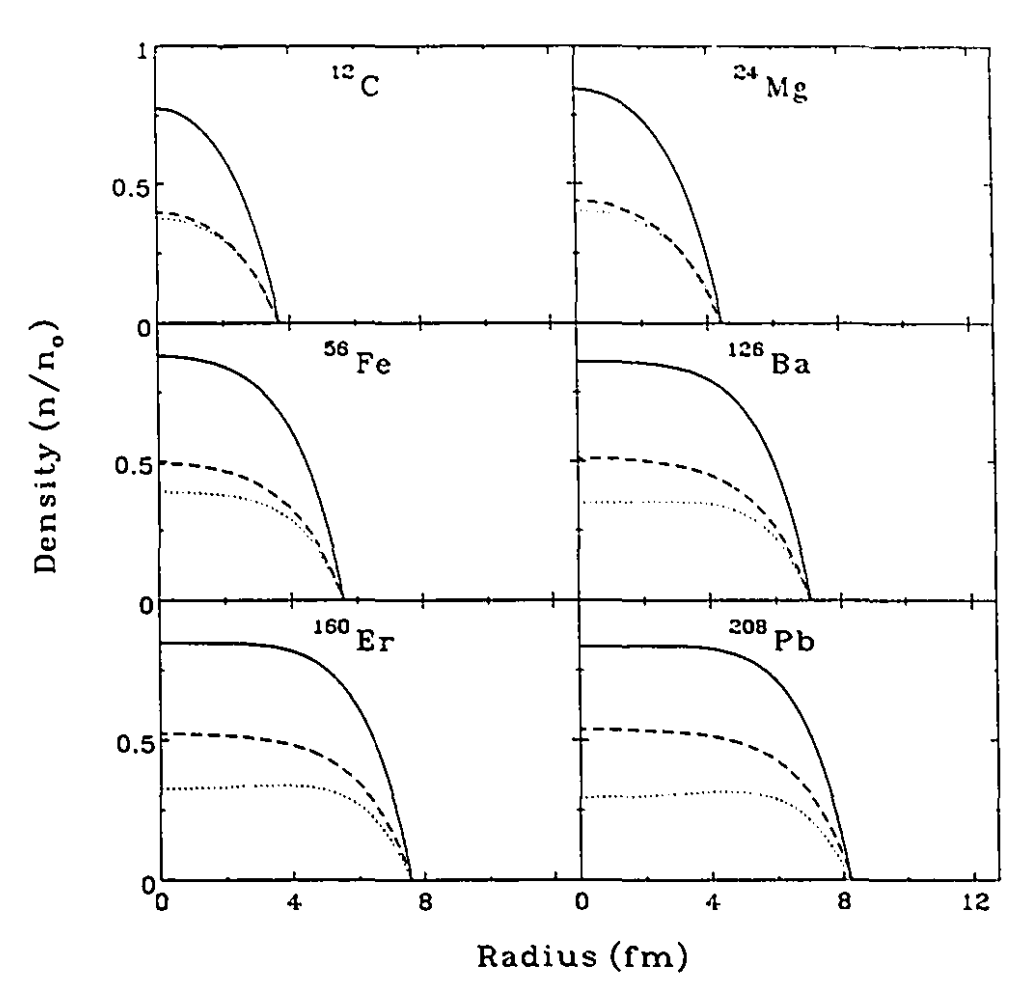


Figure 3.1: Density profiles for different nuclei using potential 1.43. Shown are the nucleon profiles (solid lines), neutron profiles (dashed lines) and proton profiles (dotted lines).

$$= -\frac{4\pi V_o a^2}{r} \left[\exp{-(r/a)} \int_0^r dr' \, r' \, \sinh(r'/a) \, n(r') + \sinh(r/a) \int_0^\infty dr' \, r' \, \exp{-(r/a)} \, n(r') \right]$$
(3.17)

where we have expanded $\frac{\exp{-|\boldsymbol{r}-\boldsymbol{r}'|/a}}{|\boldsymbol{r}-\boldsymbol{r}'|/a}$ in terms of spherical harmonics ([42], page 741), and $j_l(ix)$ and $h_l(ix)$ are the spherical Bessel functions of a complex argument. Thus we have reduced eqs. 3.8, 3.14 and 3.15 to one-dimensional equations.

We implement the above procedure by dividing the r-component in configuration space into cells of length 0.025 fm and starting with a spherical nucleus of uniform

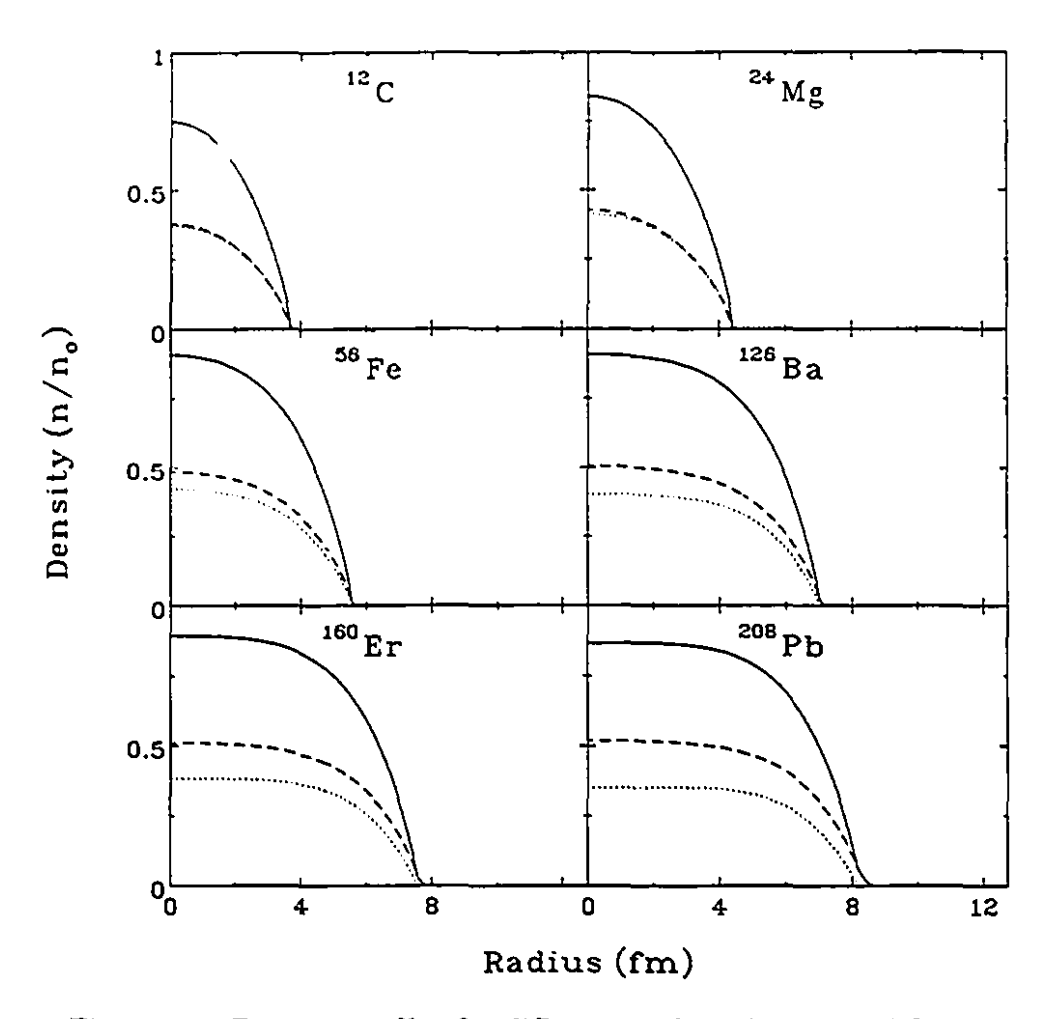


Figure 3.2: Density profiles for different nuclei using potential 1.49. Shown are the nucleon profiles (solid lines), neutron profiles (dashed lines) and proton profiles (dotted lines).

density n_o . The Coulomb and Yukawa term were calculated using eqs. 3.16 and 3.17. The accuracy demanded for the relative difference between the integrated nucleon count (or the neutron and proton counts) and \mathcal{A} (or \mathcal{N} and \mathcal{Z}) was 10^{-5} . Two successive values of the chemical potentials λ (or λ_n and λ_p) were considered equal if the relative change was less than 10^{-5} .

Once the density profiles n(r) (or $n_n(r)$ and $n_p(r)$) are known, we can calculate all the interesting variables of the system. In fig. 3.1 and 3.2 we show the density profiles for different nuclei using potentials 1.43 and 1.49 respectively. Two of the

main differences between these two potentials can be seen in the case of the heavy nuclei ¹⁶⁰Er and ²⁰⁸Pb. The first is that for potential 1.43, the proton density does not have its maximum at the origin, but rather close to the nuclear surface. This will have implications in the behaviour of rotating nuclei, as will be seen in the next section. The second difference is that for potential 1.49, the neutron profiles extend beyond the proton ones. This is reminiscent of the neutron skin observed in experiments.

3.2 Thomas-Fermi solutions for rotating nuclei

3.2.1 TF equations for rotating nucleus

The problem we now want to solve is to find Thomas-Fermi solutions for nuclei with a specified angular momentum. As for the static solutions, we want to find the solution that will minimize eq. 3.1, subject to the constraints eq. 3.2 and:

$$\int d\mathbf{r} d\mathbf{p} f(\mathbf{r}, \mathbf{p})(xp_y - yp_x) = \mathcal{L}_z$$
 (3.18)

where we have assumed that the z-axis is the axis of rotation and for the moment we consider only symmetric nuclei with no Coulomb interaction. Again, introducing Lagrange multipliers, the quantity to minimize now is:

$$\mathcal{E}' = \int d\mathbf{r} d\mathbf{p} f(\mathbf{r}, \mathbf{p}) \frac{p^2}{2m} + \int d\mathbf{r} \, \mathcal{V}(\mathbf{r}) + \lambda \left(\mathcal{A} - \int d\mathbf{r} \, n(\mathbf{r}) \right) + \omega \left(\mathcal{L}_z - \int d\mathbf{r} \, d\mathbf{p} \, f(\mathbf{r}, \mathbf{p}) (x p_y - y p_x) \right)$$
(3.19)

Since the nucleus is rotating, it is clear that at any point r, the average momentum will not necessarily be 0, i.e.:

$$\langle \boldsymbol{p} \rangle \equiv \int d\boldsymbol{p} f(\boldsymbol{r}, \boldsymbol{p}) \boldsymbol{p} \neq 0$$
 (3.20)

This can be whileved by assuming that at every point r, the Fermi sphere will be displaced by an amount p'(r):

$$f(\boldsymbol{r}, \boldsymbol{p}) = \frac{g}{h^3} \Theta(p_F(\boldsymbol{r}) - |\boldsymbol{p} - \boldsymbol{p}'(\boldsymbol{r})|)$$
(3.21)

Let us now perform the momentum integration in eq. 3.19. If we change the integration variable to q = p - p'(r) the integral becomes (suppressing for the moment the r coordinate):

$$I(\mathbf{p}') = \frac{g}{h^3} \int d\mathbf{q} \,\Theta(p_F - q) \left(\frac{(\mathbf{q} + \mathbf{p}')^2}{2m} - \omega [x(q_y + p'_y) - y(q_x + p'_x)] \right)$$

$$= \frac{4\pi g}{h^3} \left[\frac{p_F^3}{3} \left(\frac{\mathbf{p}'^2}{2m} - \omega (x p'_y - y p'_x) \right) + \frac{1}{5} \frac{p_F^3}{2m} \right]$$
(3.22)

Since this is the only term in eq. 3.19 that depends on p', we can immediately perform the minimization with respect to the latter:

$$\delta I(p') = \left(\frac{p'_x}{m} - \omega y\right) \delta p'_x + \left(\frac{p'_y}{m} + \omega x\right) \delta p'_y + \frac{p'_z}{m} \delta p'_z = 0$$
 (3.23)

which leads to

$$\mathbf{p}'(\mathbf{r}) = -m\omega y\hat{\imath} + m\omega x\hat{\jmath} + 9\hat{\mathbf{k}} = m\omega r_{\perp}\hat{\phi}$$
 (3.24)

where we have defined $r_{\perp}^2 = x^2 + y^2$. Note that the second order variation of I(p') with respect to p' is positive semi-definite, and therefore we are indeed at a local minimum. Substituting back into I(p') and using eq. 3.5 we get:

$$I(\mathbf{p}') = \frac{4\pi g}{h^3} \left[\frac{1}{2} m \omega^2 r_{\perp}^2 \left(-\frac{p_F^3}{3} \right) + \frac{p_F^5}{10m} \right]$$
$$= \frac{3h^2}{10m} \left(\frac{3}{4\pi g} \right)^{2/3} n(\mathbf{r})^{5/3} - \frac{1}{2} m \omega^2 r_{\perp}^2 n(\mathbf{r})$$
(3.25)

Substituting back into eq. 3.19 we now have:

$$\mathcal{E}' = \int d\mathbf{r} \left[\frac{3h^2}{10m} \left(\frac{3}{4\pi g} \right)^{2/3} n(\mathbf{r})^{5/3} - \frac{1}{2} m\omega^2 r_{\perp}^2 n(\mathbf{r}) + \mathcal{V}(\mathbf{r}) - \lambda n(\mathbf{r}) \right] + \lambda \mathcal{A} + \omega \mathcal{L}_z$$
(3.26)

The first order change in \mathcal{E}' under the variation $n(r) \to n(r) + \delta n(r)$ is then

$$\delta \mathcal{E}' = \int d\mathbf{r} \left[\frac{h^2}{2m} \left(\frac{3n(\mathbf{r})}{4\pi g} \right)^{2/3} - \frac{1}{2} m \omega^2 r_{\perp}^2 + \mathcal{U}(\mathbf{r}) - \lambda \right] \delta n(\mathbf{r})$$
 (3.27)

As for the static case, the above expression will only be 0 for arbitrary $\delta n(r)$ if the term in square brackets is itself 0, which gives us the condition:

$$\frac{h^2}{2m} \left(\frac{3n(r)}{4\pi g} \right)^{2/3} - \frac{1}{2} m\omega^2 r_{\perp}^2 + \mathcal{U}(r) - \lambda = 0$$
 (3.28)

Let us now return to the expressions for the angular momentum and the energy of our system and substitute for f(r,p) and p'(r). From eq. 3.18 we get, changing the momentum integration to q = p - p'(r):

$$\mathcal{L}_{z} = \int d\mathbf{r} d\mathbf{q} \frac{g}{h^{3}} \Theta(p_{F} - q) [x(q_{y} + p'_{y}) - y(q_{x} + p'_{x})]$$

$$= \frac{4\pi g}{h^{3}} \int d\mathbf{r} d\mathbf{q} \Theta(p_{F} - q) q^{2} [xp'_{y} - yp'_{x}]$$

$$= \frac{4\pi g}{h^{3}} \int d\mathbf{r} \frac{p_{F}(\mathbf{r})^{3}}{3} [x(m\omega x) - y(-m\omega y)] = m\omega \int d\mathbf{r} n(\mathbf{r}) [x^{2} + y^{2}]$$

$$= m\omega \int d\mathbf{r} n(\mathbf{r}) r_{\perp}^{2} \equiv \omega \mathcal{I}$$
(3.29)

where \mathcal{I} is the moment of inertia of the system. Similarly, the kinetic energy term in eq. 3.1 becomes:

$$\int d\mathbf{r} d\mathbf{p} f(\mathbf{r}, \mathbf{p}) \frac{p^2}{2m} = \int d\mathbf{r} d\mathbf{q} \frac{g}{h^3} \Theta(p_F - q) \frac{(\mathbf{q} + \mathbf{p}')^2}{2m}$$
$$= \frac{1}{2m} \frac{4\pi g}{h^3} \int d\mathbf{r} \left(\frac{p_F^5}{5} + \frac{p_F^3}{3} \mathbf{p}'^2 \right)$$

$$= \frac{1}{2m} \frac{4\pi g}{h^3} \int d\mathbf{r} \frac{p_F(\mathbf{r})^5}{5} + \frac{1}{2m} \int d\mathbf{r} \, n(\mathbf{r}) m^2 \omega^2 r_\perp^2$$

$$= \frac{1}{2m} \frac{4\pi g}{h^3} \int d\mathbf{r} \, \frac{p_F(\mathbf{r})^5}{5} + \frac{1}{2} \omega^2 \mathcal{I}$$

$$= \frac{1}{2m} \frac{4\pi g}{h^3} \int d\mathbf{r} \, \frac{p_F(\mathbf{r})^5}{5} + \frac{\mathcal{L}_z^2}{2\mathcal{I}}$$
(3.30)

where in the last line we have substituted for ω from the previous equation. It is now clear that the Lagrange multiplier ω can be identified with the angular velocity.

As for the static case, for non-symmetric systems the derivation is the same and we get the two coupled equations:

$$\frac{h^2}{2m} \left(\frac{3n_{\rm n}(\boldsymbol{r})}{4\pi g} \right)^{2/3} - \frac{1}{2} m\omega^2 r_{\perp}^2 + \mathcal{U}_{\rm n}(\boldsymbol{r}) - \lambda_{\rm n} = 0 \qquad (3.31)$$

$$\frac{h^2}{2m} \left(\frac{3n_p(\boldsymbol{r})}{4\pi g} \right)^{2/3} - \frac{1}{2} m\omega^2 r_\perp^2 + \mathcal{U}_p(\boldsymbol{r}) - \lambda_p = 0 \qquad (3.32)$$

3.2.2 Numerical implementation

The numerical procedure we use to solve eq. 3.28 (or eqs. 3.31 and 3.32) is similar to the one for the static solutions, but two more steps are necessary. For every angular momentum \mathcal{L}_z for we which we want a solution, we start from an initial density distribution (in most cases a previous solution at a different value of \mathcal{L}_z or, for small values of \mathcal{L}_z , from the static solution) and a guessed value for λ , and we proceed as follows:

- 1. From the current density distribution, we calculate the moment of inertia, and using eq. 3.29, we calculate ω .
- 2. From the current density profile, we calculate the finite range components of the potential (Yukawa and Coulomb terms).

- 3. Using the current value of λ and ω , we use eq. 3.28 to calculate the density n(r) at every point r.
- 4. We integrate the density profile n(r) to obtain the total number of nucleons and compare it to A, modifying λ and loop back to the previous step until both numbers agree within the prescribed accuracy.
- 5. Loop back to step 2 until two successive iterations give the same λ .
- 6. Loop back to step 1 until two successive iterations give the same ω .

This procedure was implemented by dividing configuration space into cubic cells of volume (0.5 fm)³. Because of the reflection symmetries of the equations and of the solutions sought, we only worked in the first quadrant. The Coulomb and Yukawa terms in the potential calculated by solving the associated differential equations as mentioned in section 2.6.

The self-consistency condition expressed in eq. 3.28 (or eqs. 3.31 and 3.32) is axially symmetric. Thus if the initial densities n(r) (or $n_n(r)$ and $n_p(r)$) are also axially symmetric, the solutions found for any angular momentum will also be axially symmetric. This family of solutions we labeled as the axial solutions. But we know from experiment that non-axial shapes exist. To generate them we must start with initial densities that are non-axial. In our study, we found two different families of non-axial shapes. One was the triaxial family, which we generated by starting with an ellipsoid whose axis ratios were 1.1:1:0.9, with the short axis aligned along the z-axis and the long axis along the x-axis. The other, labeled saddle-shape family, was generated from two equal mass spheres barely touching at the origin, with their centers aligned along the x-axis and rotating about the z-axis.

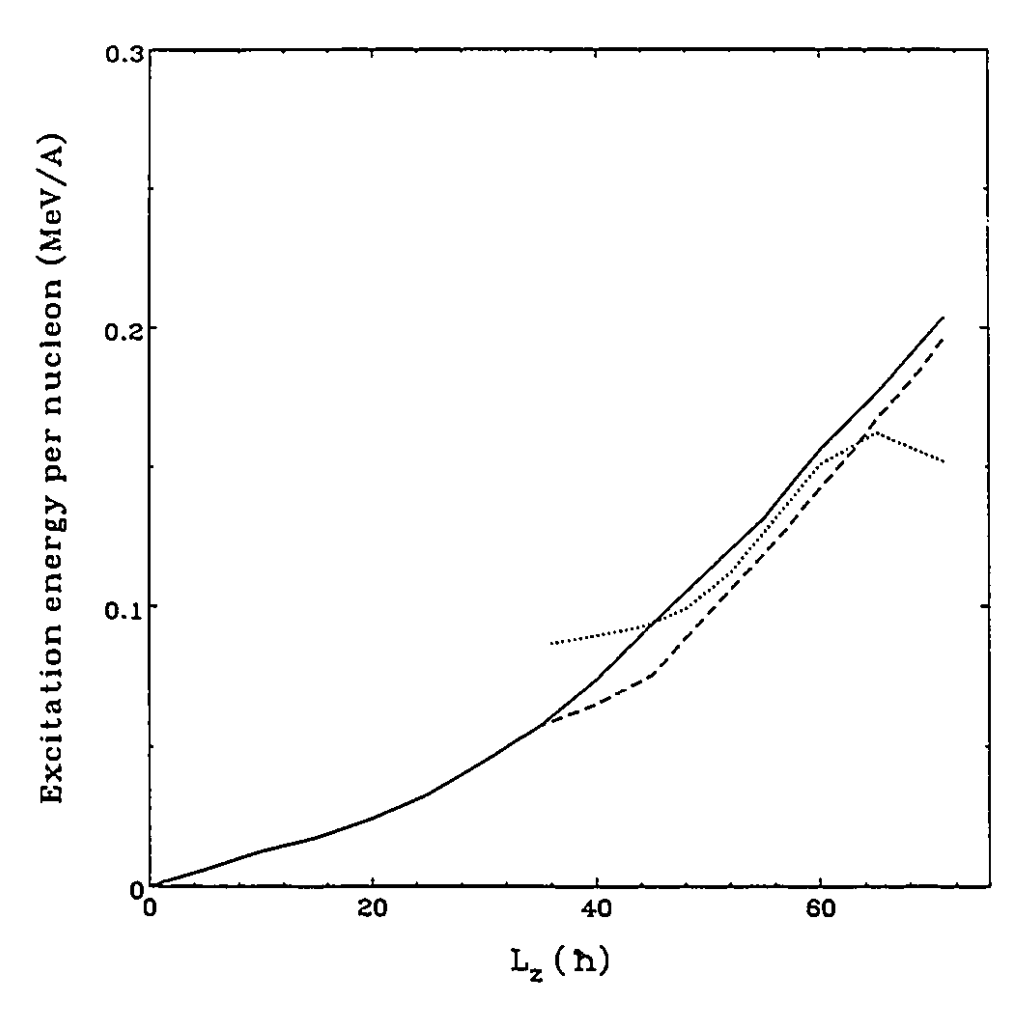


Figure 3.3: Evolution of the excitation energy per nucleon with angular momentum for ¹⁶⁰Er subject to potential 1.43. The solid line is the axial family, the dashed line is the triaxial family and the dotted line is the saddle-shaped family.

	\mathcal{L}_{t}	$\mathcal{L}_{\mathbf{s}}$	\mathcal{L}_{b}	
²⁴ Mg (1.43)		15 ħ	22 ħ	
¹²⁶ Ba (1.43)	25 ħ	55 ħ	70 ħ	
¹⁶⁰ Er (1.43)	35 π	63 ħ	72 ħ	
²⁴ Mg (1.49)	-	15 ħ	22 ħ	
¹²⁶ Ba (1.49)	25 ħ	70 ħ	93 ħ	
¹⁶⁰ Er (1.49)	45 ħ	80 ħ	90 ħ	

Table 3.1: Values of the transition values \mathcal{L}_t , \mathcal{L}_n and \mathcal{L}_b for different nuclei. The number in parenthesis indicates the potential used.

For all the nuclei studied, we observed the following behaviour: for low values of \mathcal{L}_z , the axial family is the only one that exists. As the angular momentum is increased, the rotation axis becomes shorter and the oblate shape is accentuated. The other two families appear at higher values of \mathcal{L}_z , but the axial family is the lowest in energy. A transition occurs at $\mathcal{L}_z = \mathcal{L}_s$ when the saddle shape family becomes the lowest in energy. As \mathcal{L}_z increases further the dumb-bell shape is accentuated, and at a critical value $\mathcal{L}_z = \mathcal{L}_b$ the nucleus breaks up into two equal mass nuclei. Note that the axial solutions continue to exist up to much higher values of the angular momentum. For masses greater than ~ 40 another transition occurs at $\mathcal{L}_z = \mathcal{L}_t < \mathcal{L}_s$ when the triaxial shapes become the lowest in energy. This general behaviour is illustrated in figs. 3.3 and 3.4 where we have plotted the excitation energies for $^{160}\mathrm{Er}$ as a function of angular momentum and the density contours for ¹²⁶Ba also as a function of \mathcal{L}_z . In table 3.1 we quote the values of \mathcal{L}_t , \mathcal{L}_s and \mathcal{L}_b for the nuclei we have studied (24Mg, 126Ba and 160Er, for both potentials 1.43 and 1.49). Note that the values of \mathcal{L}_{s} and \mathcal{L}_b for ¹²⁶Ba and ¹⁶⁰Er are lower for potential 1.43 than for 1.49. This is related to the behaviour of proton density profiles for heavy nuclei mentioned at the end of the previous section. Subject to potential 1.43, protons are more likely to migrate towards the surface of the nucleus than when subject to potential 1.49. As a result

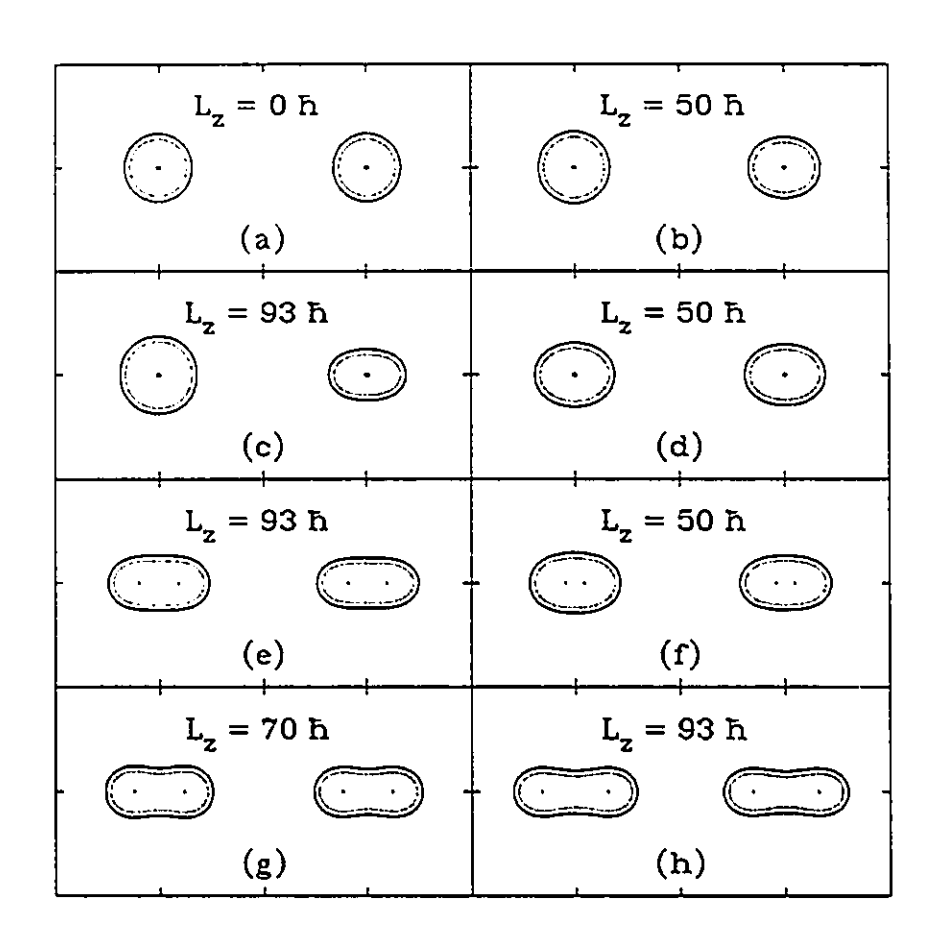


Figure 3.4: 126 Ba density contours for the three shape families: axial, (a), (b) and (c), triaxial, (d) and (e), and saddle shaped, (f), (g) and (h). We used potential 1.49 for this calculation. In each frame, the contour on the left is a cut along the x-y plane and the one on the right along the x-z plane, with the x-axis running horizontally in both cases (the tick marks are 10 fm apart).

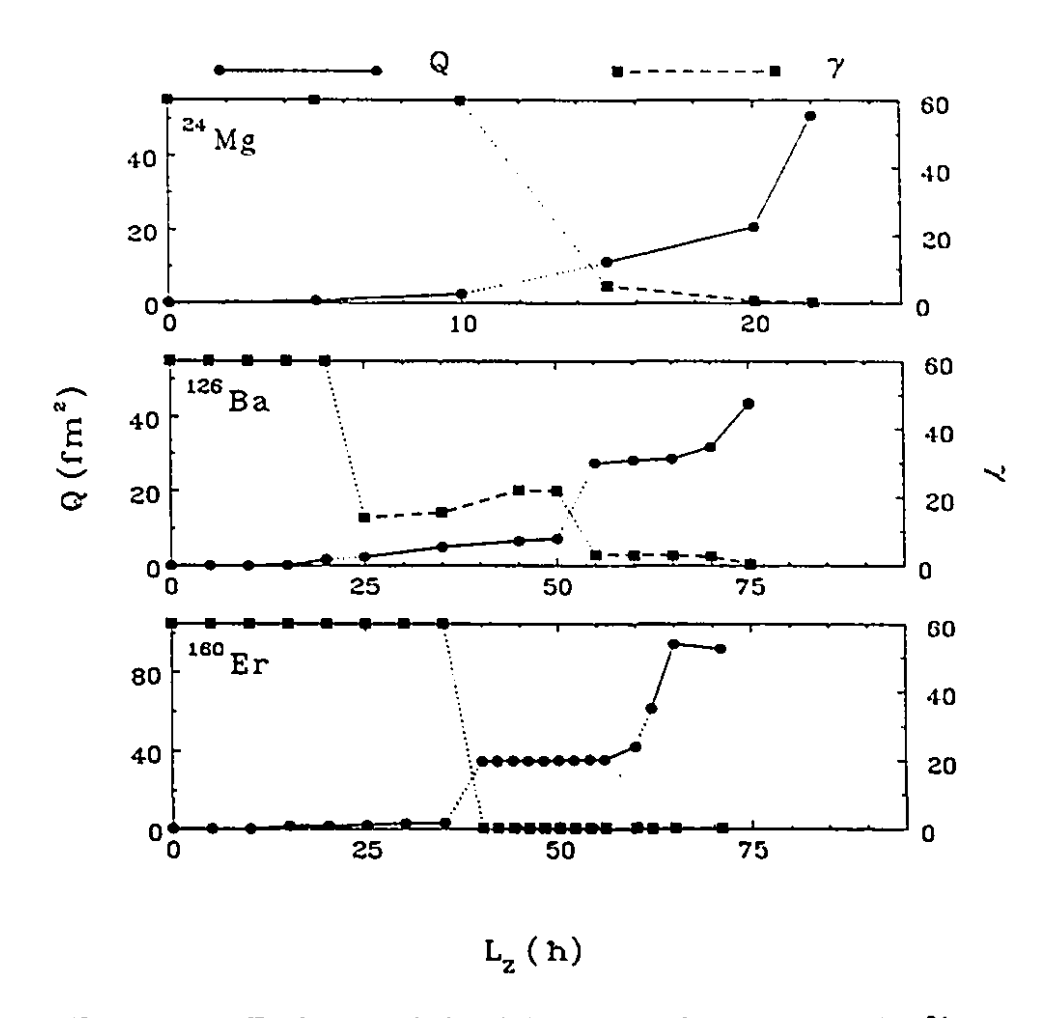


Figure 3.5: Evolution of the deformation characteristics for 24 Mg, 126 Ba and 160 Er using potential 1.43. The quadrupole moment Q is represented by the solid lines and circles (left hand side scale) and γ by the dashed lines and squares (right hand side scale). The dotted lines indicate the transitions at which a different family becomes lowest in energy. Note that the γ values for 160 Er's triaxial families are very small.

of this, at higher angular momenta the nucleus can withstand higher elongations at a lower energy cost. Thus the lower values of \mathcal{L}_{a} and \mathcal{L}_{b} for the first potential.

The deformation characteristics for the potential 1.43 are shown in fig. 3.5 for 24 Mg, 126 Ba and 160 Er. In this figure we have used $Q\cos\gamma = \langle 2z^2 - x^2 - y^2 \rangle$ and $Q\sin\gamma = \langle \sqrt{3}(x^2 - y^2) \rangle$. We keep Q positive and γ in the region $0^{\circ} - 60^{\circ}$ by relabelling the axes such that $\langle z^2 \rangle \geq \langle y^2 \rangle \geq \langle x^2 \rangle$. The γ values identified here remain unchanged

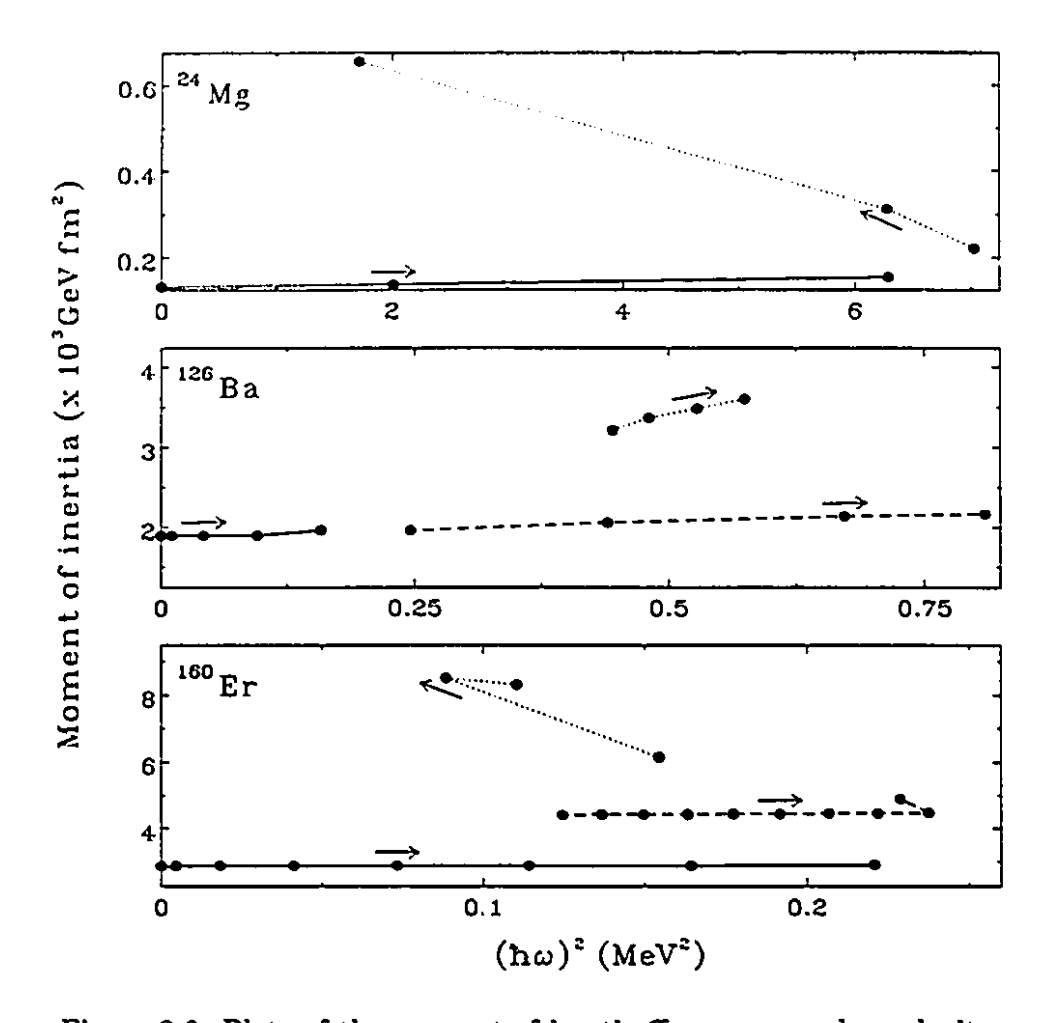


Figure 3.6: Plots of the moment of inertia \mathcal{I} versus angular velocity for ²⁴Mg, ¹²⁶Ba and ¹⁶⁰Er using potential 1.43. Only the lowest energy solutions are plotted for each angular momentum: the solid lines represent the axial solutions, the dashed lines the triaxial (not present in the case of ²⁴Mg) and the dotted lines the saddle-shaped. The arrows indicate the direction of increasing \mathcal{L}_z .

in the Lund convention.

The axial solutions which are lowest in energy in for low values of angular momentum do not correspond to what is actually found in experiment. In the ground state bands most nuclei have prolate like deformations and they do not rotate about the symmetry axis. The triaxial shapes that take over at higher angular momenta have a better chance of being realizable in nature. As mentioned earlier, these are

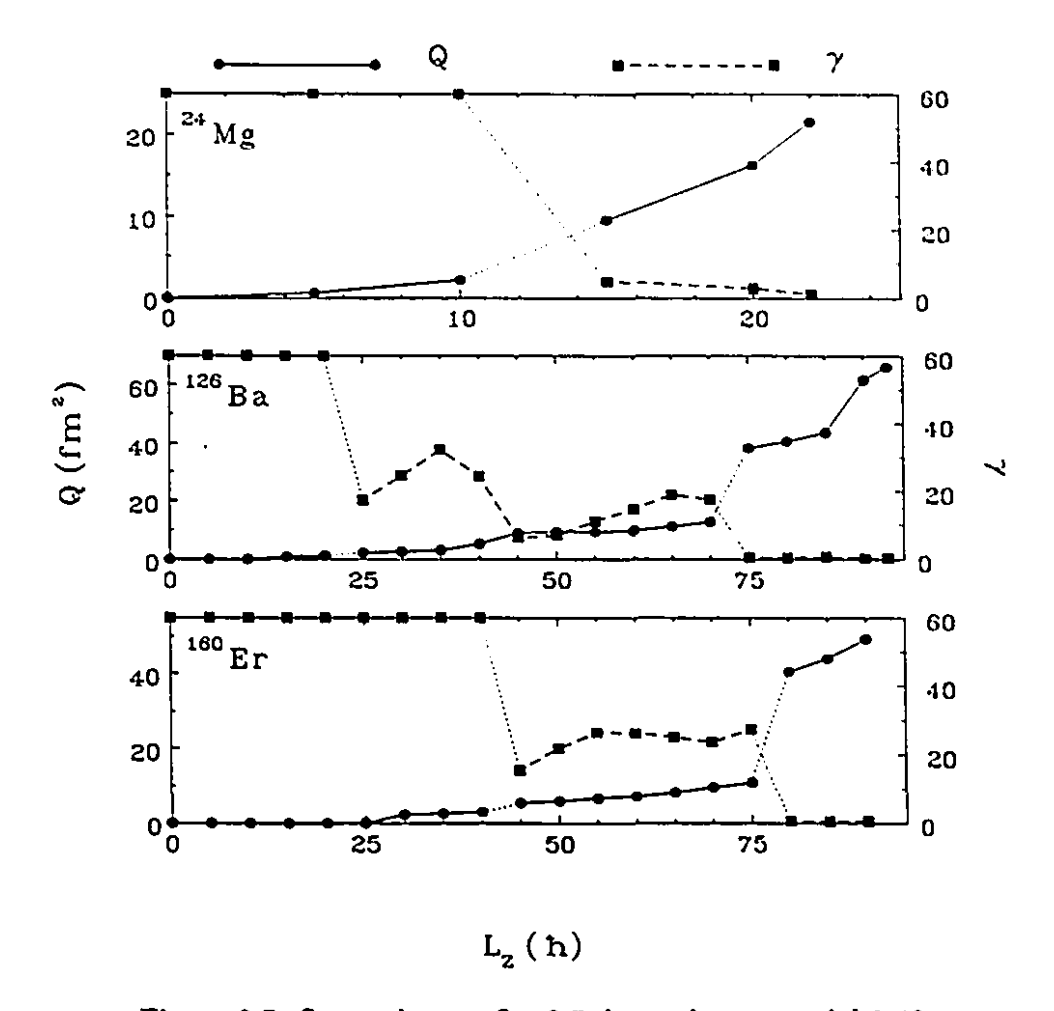


Figure 3.7: Same plots as fig. 3.5, but using potential 1.49.

prolate and rotate about their shortest axis; the super deformed bands observed in experiment are thought to have similar shapes. The triaxial shapes of ¹²⁶Ba and ¹⁶⁰Er shown in fig. 3.5 have large deformations. In the latter case, the ratio of the largest axis to the smallest axis is 2:1, whereas in the former case the ratio is 3:2. These happen to be the values found experimentally for both nuclei [46]. However, no great emphasis should be placed on these numbers because we will see that the exact numerical values depend on the potential used. Also, the saddle-shaped families have very high deformations but we do not think these are candidates for the super deformed bands: first, they become the lowest energy solutions at very high values

of \mathcal{L}_z , they only persist for a short while before they reach the fission limit, and the change of moment of inertia from one spin state to another is too great. The triaxial shapes show much more consistency in the moment of inertia. These are shown in fig. 3.6.

In fig. 3.7 we show the deformation characteristics obtained with potential 1.49. This demonstrates the sensitivity of the results to the potentials used. With this potential, the ratio of the largest to the smallest axis drops from 2:1 to 3:2 in the case of 160 Er. Also, \mathcal{L}_b has gone from 72 to 90 \hbar . We suspect that quantum effects left out in Thomas-Fermi theory will lead to a larger deformation and will therefore lower \mathcal{L}_b .

3.2.3 Comparison with other models

We will now try to establish a link between our results and the classic liquid drop results of Cohen, Plasil and Swiatecki [23]. In that paper the authors studied the evolution of liquid drop shapes and energies as a function of rotational energy, keeping their volume fixed and the density constant throughout the volume. Thus the binding energy of a liquid drop only depends on the surface energy, the Coulomb energy and the rotational energy. To identify a nucleus with a given angular momentum, the authors introduced the variables:

$$x \equiv \frac{E_{\text{coul}}^{(0)}}{2E_{\text{nur}}^{(0)}} \quad , \qquad y \equiv \frac{E_{\text{rot}}^{(0)}}{E_{\text{nur}}^{(0)}}$$
 (3.33)

the superscript 0 indicating that the surface and Coulomb energies are calculated for the ground state (spherical) solutions, and the rotation energy from the ground state shape. Note that x (the fissibility parameter) is an intrinsic property of each nucleus and y is a measure of the rotational energy. The evolution of any drop can then

be universally established for all values of these variables. Their results (for nuclear drops) can be summarized as follows:

- As L_z (y) increases, the ground state spheres become oblate, and they are the lowest energy solutions. There is a second family of shapes (the saddle-point solutions) which are also stable, but at higher energies.
- 2. At a certain value of y (y_1), the oblate solutions become unstable to triaxial deformations which become the lowest energy solutions.
- 3. At a further value y_{II} , the triaxial shapes cease to exist (there are no single-volume solutions, i.e. fission has occurred).
- 4. For x > 0.81, y_1 and y_{11} become equal.

(Note that the authors nomenclature does not correspond with our own, which comes about from the initial densities used to generate each family of shapes).

Qualitatively, we observe a similar behaviour in our solutions. In order to make more quantitative comparisons, we need to estimate the x value for our solutions, and therefore their surface energies. From our ground state Thomas-Fermi solutions we can calculate r_{90} and r_{10} , which are defined as the radii at which the density falls below 90% and 10% of the maximum density respectively. We then calculate the number of nucleons inside the shell defined by these two radii and also their energy, as well as the energy that the same number of nucleons would have in nuclear matter. We define the surface energy as the difference between the two energies (as a check, we have compared the surface energies thus obtained to the ones we would expect from the mass formula of eq. 1.50 and found that they always agree to within 5%). Thus we can determine x for each of our nuclei. To calculate the corresponding y_1 we

	x	\mathcal{L}_{I}	$\mathcal{L}_{\mathbf{s}}$	$\mathcal{L}_{ ext{II}}$	\mathcal{L}_{b}
²⁴ Mg (1.43)	0.129	14.28 π	15 ħ	23.23 π	22 π
¹²⁶ Ba (1.43)	0.575	57.56 ħ	55 ħ	64.98 ħ	70 ħ
¹⁶⁰ Er (1.43)	0.684	60.64 ħ	63 ħ	61.31 π	72 ħ
²⁴ Mg (1.49)	0.107	15.97 ħ	15 ħ	26.10 π	22 π
¹²⁶ Ba (1.49)	0.478	72.79 ħ	70 ħ	97.07 ħ	93 ħ
¹⁶⁰ Er (1.49)	0.585	80.32 ħ	80 ħ	89.29 ħ	90 ħ

Table 3.2: Values of x, \mathcal{L}_{I} , \mathcal{L}_{a} , \mathcal{L}_{II} and \mathcal{L}_{b} for the different nuclei studied (the number in parenthesis indicates the potential used). \mathcal{L}_{I} and \mathcal{L}_{II} were calculated using the interpolations from ref. 23, whereas \mathcal{L}_{a} and \mathcal{L}_{b} were extracted from our calculations.

use the interpolation [23]:

$$y_1 = 0.2829 - 0.3475x - 0.0016x^2 + 0.0501x^3$$
 for $x < 0.75$
 $y_1 = 1.4(1-x)^2 - 4.5660(1-x)^3 + 6.7443(1-x)^4$ for $x > 0.75$

Since no similar interpolation for y_{II} is given in ref. 23, we fitted the y_{II} -curve from fig. 2b in that reference and found the following fit:

$$y_{11} = 0.787 - 1.239x + 0.253x^2 - 0.989x^3 + 1.387x^4$$
 for $x < 0.55$
$$y_{11} = 3.796 - 17.499x + 31.355x^2 - 25.421x^3 + 7.770x^4$$
 for $0.55 < x < 0.81$
$$y_{11} = y_1$$
 for $x > 0.81$

We then proceed to calculate the corresponding angular momenta $\mathcal{L}(y_{\rm I}) = \mathcal{L}_{\rm I}$ and $\mathcal{L}(y_{\rm II}) = \mathcal{L}_{\rm II}$. The values of $\mathcal{L}_{\rm I}$ and $\mathcal{L}_{\rm S}$ and of $\mathcal{L}_{\rm II}$ and $\mathcal{L}_{\rm b}$ are quite similar (see table 3.2). But the transitions involved in the first case are very different in nature, and the numerical agreement is in itself surprising, since we are using an underlying nuclear force, whereas in ref. 23 the authors only consider the surface tension and the Coulomb repulsion. Also the volume constraint is a very restrictive one (in the case of ¹⁶⁰Er the volume changes by a factor of 5 just before fission).

We end our discussion with a short comparison with cranked quantum mechanical calculations [26-28]. It is clear that there is an immense difference between quantum and Thomas-Fermi solutions for low \mathcal{L}_z states. In the former, most nuclei are prolate and rotate perpendicular to the symmetry axis for the yrast low angular momentum states. In our Thomas-Fermi theory nuclei are oblate for yrast low \mathcal{L}_z states and moreover they rotate about the symmetry axis. One may hope to find better correspondence at higher angular momenta. Unfortunately, low mass nuclei break up before such high spin states are reached. Detailed quantum calculations have been done for 20 Ne [27] and 24 Mg [28]. Except for values of \mathcal{L}_z at which the nuclei disintegrate there is not much in common between Thomas-Fermi results and quantum mechanical cranking results for such light nuclei. Quantum mechanical calculations in which all orbitals are included in the cranking and not just a few "valence" orbitals are extremely time consuming for larger nuclei. The following observations are made on the basis of the calculations on 80Sr reported in ref. 26. In quantum mechanics many solutions are possible based on different occupancies of orbitals and the best that we can hope is that Thomas-Fermi solutions are in some sense an average of the quantum solutions. In ref. 26 many bands are shown; between 36 \hbar and 60 \hbar and as well as all the calculated super deformed bands have small values of γ , just as we find in our non-axial solutions. Thus in this particular example the Thomas-Fermi calculations do reproduce the average behaviour. The values of \mathcal{L}_b are also similar.

Conclusion

The extended BUU model presented in chapter 2 is one of the most complete codes used in heavy ion collisions. With fluctuations built in, high numerical accuracy, finite-range potentials and self-consistent initial density distributions, it is the only one at the moment that has been compared with experimental results. The quite remarkable agreement with the MSU results leads us to believe in the validity of the approach even at such low energies, and has established that multifragmentation is an important mode of deexitation at this energies.

Despite its success, improvements are still necessary. The most important is to include more sophisticated potentials, mainly momentum dependent potentials such as the one described in [48]. While it is relatively easy to extend the LHM to include such potentials, it's implementation presents some very serious problems, not the least of which is the computer power necessary to run such code (both in CPU time and available memory). Also, the cascade code has to be modified so that energy-conservation is guaranteed in a nucleon-nucleon collision [49]. Also one must develop a method that correctly treats the inelastic channels within the fluctuation code. Most important, more comparisons of the model with experiments at different energy regimes and with a wide variety of systems would be necessary to confirm the overall validity of the model.

The Thomas-Fermi model of nuclear rotations has given us some very useful in-

sights into the dynamics of nuclear rotations and the role played by the underlying forces. It has also allowed us to bridge the gap between the classical liquid drop model and the cranking quantum calculations. The latter have a much higher predicting power, but the simplicity of the Thomas-Fermi equations, and the relative ease with which solutions can be obtained for any nucleus (from one hour of CPU for low angular momenta to a few days for angular momenta close to the break-up value) make it an attractive exploratory tool.

Once more we emphasize that the quantitative agreement between our model and the classical calculations is most surprising, given how different the underlying assumptions are. We believe that this gives validity to the predictions of the liquid drop model. Finally, although direct comparison with experiment is not possible, we believe that the qualitative features of our solutions at large angular momenta are probably realistic, including the break up values obtained.

Appendix A

Phase-diagram for nuclear matter

We would like to calculate the phase-diagram of a fluid of A interacting nucleons enclosed in a volume V in equilibrium with a heat reservoir at temperature T. Macroscopic observables are calculated as sums over the available states s of the corresponding microscopic quantities, weighted by the Fermi-Dirac occupation probabilities:

$$f_{\rm FD}^s = \frac{1}{1 + \exp\beta(\epsilon^s - \mu)} \tag{A.1}$$

(For our system, the states can be conveniently labelled by the coordinates in configuration and momentum space and spin-isospin labels of the nucleons.) The microscopic energy ϵ^s is then simply the sum of the kinetic term κ^s plus the potential term u^s . For nuclear matter subject to Skyrme potentials (eq. 1.36) or Skyrme potentials augmented with a Yukawa term in the limit $V \to \infty$ (eq. 1.42), u^s is the same for all states s, and therefore one can redefine the chemical potential $\mu \to \mu - u$ and the sum (integral) over configuration space can be performed trivially. Then sums over states can be replaced by integrals over momentum:

$$\sum_{s} \to gV \int \frac{\mathrm{d}p}{(2\pi\hbar)^3} = g \frac{4\pi V}{(2\pi\hbar)^3} \int_0^\infty \mathrm{d}p \, p^2 \tag{A.2}$$

where g is the spin-isospin degeneracy of the nucleons. We can now easily calculate \mathcal{A} , the kinetic energy \mathcal{T} , the potential energy \mathcal{V} and the entropy \mathcal{S} of the system:

$$A = g \frac{4\pi V}{(2\pi\hbar)^3} \int_0^\infty dp \frac{p^2}{1 + \exp\beta(p^2/2m - \mu)}$$
 (A.3)

$$T = g \frac{4\pi V}{(2\pi\hbar)^3} \int_0^\infty dp \, \frac{p^4/2m}{1 + \exp\beta(p^2/2m - \mu)}$$
 (A.4)

$$V = V \left[\frac{A_g}{2} n^2 + \frac{B}{\sigma + 1} n^{\sigma + 1} \right] \tag{A.5}$$

$$S = -g \frac{4\pi V}{(2\pi\hbar)^3} \int_0^\infty dp \left[f_{\rm FD}^p \ln f_{\rm FD}^p + (1 - f_{\rm FD}^p) \ln(1 - f_{\rm FD}^p) \right] \tag{A.6}$$

where we have defined $A_g = A$ for pure Skyrme potentials, and $A_g = A + 4\pi V_o a^3$ if we include a Yukawa term. Changing the integration variable to $x = \beta(p^2/2m - \mu)$, the integrals become:

$$A = g \frac{2\pi V}{(2\pi\hbar)^3} (2mkT)^{3/2} \int_{-\beta\mu}^{\infty} dx \, \frac{(x+\beta\mu)^{1/2}}{1+\exp x}$$
 (A.7)

$$T = g \frac{2\pi V}{(2\pi\hbar)^3} (2mkT)^{5/2} \int_{-\beta\mu}^{\infty} dx \, \frac{(x+\beta\mu)^{3/2}}{1+\exp x}$$
 (A.8)

$$S = g \frac{2\pi V}{(2\pi\hbar)^3} (2mkT)^{3/2} \int_{-\beta\mu}^{\infty} dx (x + \beta\mu)^{1/2}$$

$$\times \left[\ln(1 + \exp x) - \frac{x \exp x}{1 + \exp x} \right] \tag{A.9}$$

Note that if we fix two to the observables in the above equations, all other observables can be determined. Thus, if we fix A and T, we can use eq. A.7 to determine μ , and then calculate T and S. We can also take advantage of the fact that the entropy per nucleon is only a function of $\beta\mu$ (see eqs. A.9 and A.7) to calculate the isentropes, by first solving for $\beta\mu$ and for different values of A use eq. A.7 to calculate T.

We can now calculate the pressure: the microscopic kinetic pressure p° is given by:

$$p^{s} \equiv -\frac{\partial \epsilon^{s}}{\partial V} \tag{A.10}$$

The volume dependance of ϵ^{s} is fixed by the periodicity condition on the wave number:

$$k^{s} = 2\pi V^{-1/3} [x^{s}\hat{\imath} + y^{s}\hat{\jmath} + z^{s}\hat{k}]$$
 (A.11)

Thus the total macroscopic pressure \mathcal{P} is just:

$$\mathcal{P} = \frac{2\mathcal{T}}{3V} - \frac{\partial \mathcal{V}}{\partial V} = \frac{2\mathcal{T}}{3V} + \frac{A_g}{2}n^2 + \frac{B}{\sigma + 1}n^{\sigma + 1}$$
(A.12)

We can now calculate the coexistence curve and the isothermal and adiabatic spinodals for nuclear matter. The latter curves are defined as the set of loci in the phase-diagram of pressure extrema along the isothermals and the isentropes respectively. The coexistence curve defines the region of the phase-diagram where both phases of the fluid are in chemical equilibrium, and it is determined using Maxwell's construction. The relevance of these curves is discussed in sec. 1.4.

References

- [1] S. Das Gupta and A. Z. Mekjian, Phys. Reports 137 72 (1981) 131.
- [2] W. G. Lynch and W. A. Friedman, Phys. Rev. C28 (1983) 16.
- [3] J. Cugnon, T. Mizutani and J. Vandermeulen, Nucl. Phys. A352 (1981) 505.
- [4] E. A. Uehling and G. E. Uhlenbeck, Phys. Rev. 43 (1933) 552.
- [5] G. F. Bertsch, H. Kruse and S. Das Gupta, Phys. Rev. C93 (1984) 673.
- [6] G. F. Bertsch and S. Das Gupta, Phys. Reports 160 (1988) 189.
- [7] J. Aichelin, G. Peilert, A. Bohnet, A. Rosenhauer, H. Stöcker and W. Greiner, Phys. Rev. C37 (1988) 2451.
- [8] D. H. Boal and J. N. Glosli, Phys. Rev. C38 (1988) 2621.
- [9] W. Bauer, G. F. Bertsch and S. Das Gupta, Phys. Rev. Lett. 58 (1987) 863.
- [10] S. Ayik, in Proceedings of the Workshop on Nuclear Dynamics VI, Jackson Hole, Wyoming (1990), edited by J. Randrup (Report LBL-28709).
- [11] J. Randrup and B. Remaud, Nucl. Phys. A514 (1990) 339.
- [12] R. Lenk and V. Pandharipande, Phys. Rev. C39 (1989) 2242.
- [13] A. Bonasera, M. di Toro and C. Gregoire, Nucl. Phys. A463 (1987) 653.
- [14] C. Gregoire, B. Remaud, F. Seville and L. Vinet, Phys. Lett. 186 (1987) 14.
- [15] P. Bonche, S. E. Koonin and J. W. Negele, Phys. Rev. C13 (1976) 1226.
- [16] H. H. Gan, S. J. Lee and S. Das Gupta, Phys. Rev. C86 (1987) 2365.
- [17] C. Gregoire, B. Remaud, F. Seville, L. Vinet and Y. Raffray, Nucl. Phys. A186 (1987) 317. (1987) 14.

- [18] S. J. Lee, H. H. Gan, E. D. Cooper and S. Das Gupta, Phys. Rev. C40 (1989) 2585.
- [19] D. Horn et al., Contribution to the 6th Nordic Meeting on Nuclear Physics, 1989 (Kopervik, Norway, 1989)
- [20] C. Pruneau et al., Nucl. Phys. A534 (1991), 204.
- [21] R. G. Seyler and C. H. Blanchard, Phys. Rev. 124 (1961) 227.
- [22] W. D. Myers and W. J. Swiatecki, Ann. Phys. (NY) 204 (1990) 401.
- [23] S. Cohen, F. Plasil and W. J. Swiatecki, Ann. Phys. 829 (1974) 557.
- [24] A. J. Sierk, Phys. Rev. C33 (1986) 2039.
- [25] S. Åberg, H. Floccard and W. Nazarewicz, Annu. Rev. Nucl. Part. Sci. 40 (1990) 439.
- [26] P. Bonche, H. Flocard and P. H. Heenen, Nucl. Phys. A523 (1991) 300.
- [27] P. Bonche, H. Flocard and P. H. Heenen, Nucl. Phys. A467 (1987) 115.
- [28] H. Flocard, P. H. Heenen, S. J. Krieger and M. S. Weiss, Nucl. Phys. A391 (1982) 285.
- [29] A. Bohr and B. R. Mottelson, Nuclear structure, Vol. 2 (Benjamin, New York, 1975) ch. 4.
- [30] M. A. Preston and R. K. Badhuri Structure of the nucleus (Addison-Wesley, Reading, MA, 1975) ch. 9.
- [31] G. F. Bertsch, in: Frontiers of Nuclear Dynamics, eds. R. Broglia and C. H. Dasso (Plenun Press, 1985) p. 27.
- [32] G. F. Bertsch and P. J. Siemens, Phys. Lett. 126B (1983) 9.
- [33] B. K. Jennings and A. D. Jackson, Phys. Reports 66 (1980) 141.
- [34] C. Y. Wong, Phys. Rev. C25 (1982) 14661.
- [35] S. Das Gupta, C. Gale and J. Gallego, Phys. Rev C33 (1986) 1634.
- [36] S. Das Gupta, C. Gale, J. Gallego, H. H. Gan and R. D. Ratna-Raju, Phys. Rev. C 35 (1987) 556.

- [37] J. Cugnon, Phys. Lett. 135B (1984) 377.
- [38] W. H Press, B. P. Flannery, S. A. Teukolsky and W. T. Vetterling, Numerical Recipes (Cambridge University Press, 1986) pp 615-667.
- [39] S. E. Koonin, K. R. T. Davies, V. Maruhn-Rezwani, H. Feldmeier, S. J. Kreiger and J. W. Negele, Phys Rev C15 (1977) 1359.
- [40] S. Gilbert, MSc Thesis, Université Laval, 1990.
- [41] G. Fai and J. Randrup, Nucl. Phys. A404, (1983) 551.
- [42] J. D. Jackson, Classical Electrodynamics, 2nd Edition (John Wiley & Sons, New York, 1975).
- [43] W. D. Myers, Nucl. Phys. A296 (1978) 177.
- [44] G. Cecil, S. Das Gupta and W. D. Myers, Phys. Rev. C22 (1980) 2018.
- [45] J. Gallego and S. Das Gupta, Phys. Lett. B270 (1991) 6.
- [46] J. Waddington, private communication.
- [47] J. M. Eisenberg and W. Greiner, Nuclear Models, Vol. 1, 3rd Edition (North Holland, Amsterdam, 1987) p. 727.
- [48] G. M. Welke, M. Prakash, T. T. Kuo, S. Das Gupta and C. Gale, Phys. Rev. C38 (1988) 2101.
- [49] C. Gale and S. Das Gupta, Phys. Rev. C42 (1990) 1577.